

Can the Oxygen $2p$ Band Be Hole Doped?

Thi Ngoc Huyen Vu[†] and Yu Kumagai^{*,†,‡}

[†]*Institute for Materials Research, Tohoku University, Sendai, Miyagi 980-8577, Japan*

[‡]*Division for the Establishment of Frontier Sciences, Organization for Advanced Studies,
Tohoku University, Sendai, Miyagi 980-8577, Japan*

E-mail: yukumagai@tohoku.ac.jp

Abstract

The development of p -type oxide semiconductors remains impeded by the inherently low-lying valence-band maximum (VBM) dominated by O- $2p$ states. A prevailing approach to mitigate this limitation is to elevate the VBM by introducing cation states that hybridize with O- $2p$ orbitals or lie energetically above the O- $2p$ level. Nevertheless, the p -type oxides reported to date exhibit limited hole mobilities. To expand the search space, it is essential to accurately understand the intrinsic difficulty of introducing holes into O- $2p$ orbitals. Accordingly, we evaluated 845 oxides to identify those in which holes can be doped into O- $2p$ bands. Our high-throughput screening revealed CaCdO₂ as the only promising exemplar, in which the VBM is slightly hybridized with deep-lying Cd- $3d$ states. Our screening suggests that hole doping into O- $2p$ orbitals is extremely difficult and thus reinforces the effectiveness of the traditional “VBM-raising strategy.”

Introduction

Oxide materials are attractive due to their chemical stability and ease of synthesis under ambient conditions. In particular, oxide semiconductors are a technologically important

class of materials with wide range of applications in displays,¹ transparent devices,² power devices,³ catalysis,⁴ and photocatalysis.⁵ However, a longstanding challenge remains: while several *n*-type oxide semiconductors (e.g., InGaZnO,⁶ Ga₂O₃,³ ZnO,⁷ In₂O₃,⁸ and SnO₂⁹) are well established in consumer electronics, *p*-type oxides are absent from practical applications despite extensive research.^{10–12} This asymmetry originates from the difficulty of *p*-type doping in oxides, in which the valence bands are typically dominated by deep O-2*p* orbitals with little dispersion, leading to higher acceptor formation energies and hole compensation by oxygen vacancies.¹³

A common strategy for achieving hole dopability in oxides is to raise the valence band maxima (VBM) by either hybridizing other orbitals with O-2*p* orbitals or introducing orbitals energetically above the O-2*p* levels.^{11,12,14,15} In this study, we refer to this as the traditional “VBM-raising strategy.” For example, CuAlO₂, the first *p*-type transparent conducting oxide (TCO), shows hole conductivity due to strong hybridization between fully occupied Cu-3*d* and O-2*p* states.¹⁶ Similar behavior is observed in other Cu-based delafossites.^{17–20} The latter case includes SnO, PbO, BaBiO₃, and TeO₂, where lone-pair orbitals from cations such as Sn²⁺, Pb²⁺, Bi³⁺ or Te⁴⁺ lie above the CBM.^{21–24} The mixture of these two approaches involves introducing partially filled *d* orbitals, as seen in compounds like NiO,^{25,26} Cr₂O₃,²⁷ LaVO₃,²⁸ and V₂O₃.²⁹ Many *p*-type TCOs proposed in theoretical studies have also been suggested based on the VBM-raising strategy.^{10,11,14}

While this strategy is well-founded, expanding the effective search for *p*-type oxides remains necessary because representative *p*-type oxides reported previously exhibit low hole mobilities (e.g., hole mobilities of 0.25 and 18.71 in CuAlO₂³⁰ and cm² V⁻¹ s⁻¹ SnO,³¹ respectively, vs electron mobilities of 200–250 cm² V⁻¹ s⁻¹ and 125–200 in ZnO³² and SnO₂³³), respectively. To address this, a precise understanding of the intrinsic difficulty of introducing holes into O-2*p* orbitals is essential. For example, holes are mostly compensated by charged oxygen vacancies.³⁴ However, our high-throughput calculations on oxygen vacancies reveal that the formation energies in the +2 charge state span as much as 9.5 eV.³⁵ This indicates

that some oxides may resist hole compensation by the oxygen vacancies due to their high formation energies, even when the Fermi level lies near the deep VBM composed of the O-2*p* orbitals. Therefore, we aim to identify if there are oxides, from 845 candidates, where holes can be introduced into the O-2*p* bands. Such insights should provide important design guidelines for the future exploration of *p*-type TCOs.

Our workflow is illustrated in Fig. 1. First, we screen oxides based on the formation energies of oxygen vacancies. Next, we quantify the orbital contributions to the VBM of the screened oxides and retain those whose VBM are primarily composed of the O-2*p* orbitals. We then discuss the acceptor levels introduced by cationic dopants in the remaining oxides. Finally, we evaluate the formation energies of native defects and acceptor dopants in the screened oxides using the HSE06 hybrid functional, in order to investigate the hole dopability of the O-2*p* bands.

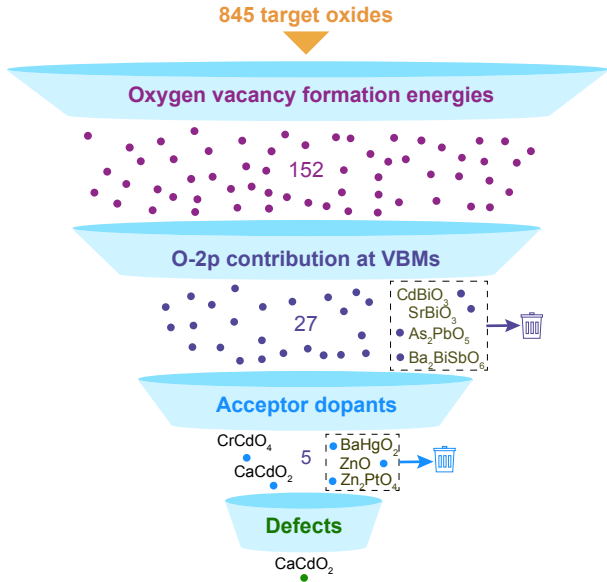


Figure 1: Flow to screen oxides that can be hole doped into the O-2*p* bands in this research. The remaining numbers of oxides in each step are also shown. The oxides enclosed in the dashed box were excluded from the screening based on a detailed analysis of their VBM character (see text). The 152 oxides considered in the second step are listed in Table S1–S3 in the Supporting Information, based on the O-2*p* contribution at the VBM.

Results and discussion

Oxygen vacancy formation energies

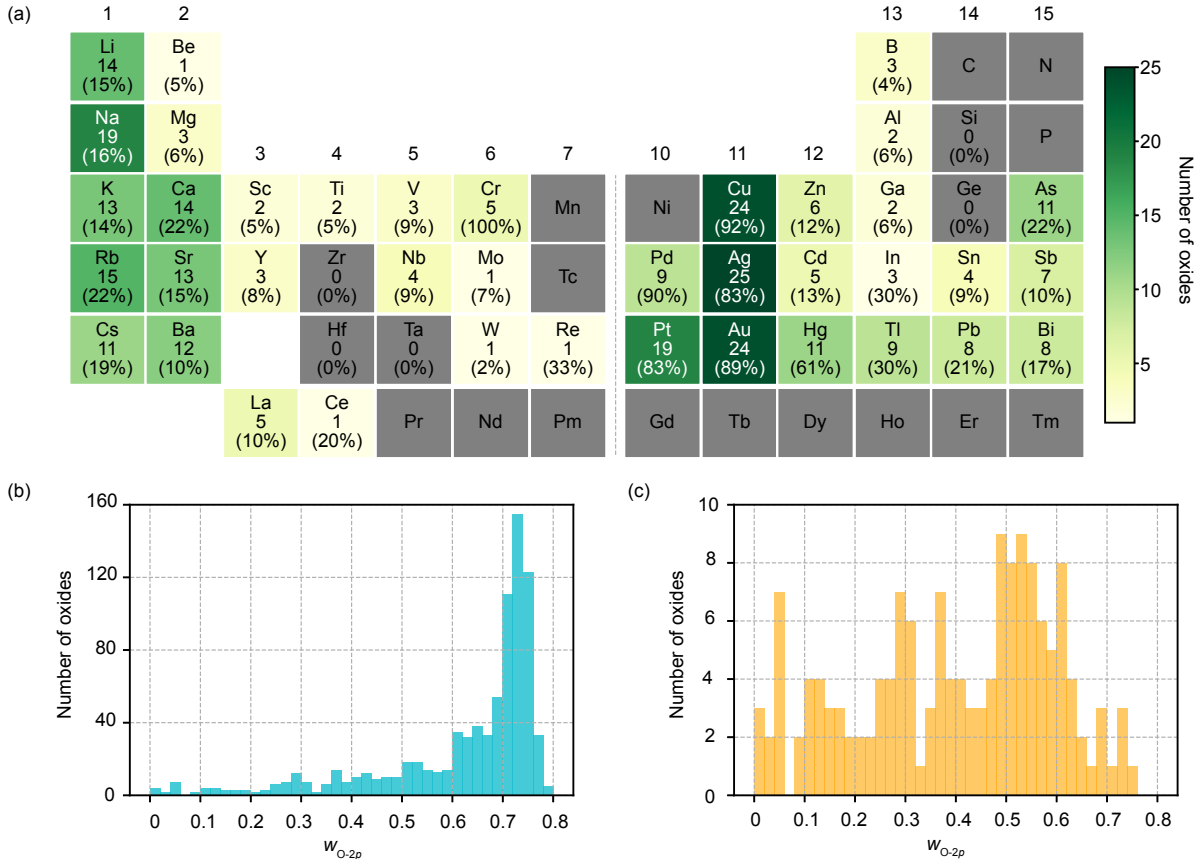


Figure 2: (a) Number of oxides containing each element among the 152 oxides retained after screening based on oxygen vacancy formation energies. The percentages in parentheses indicate the survival rates after screening. The number of oxides containing each element before the screening are shown in the Supporting Information. (b, c) Histogram of the O-2p contribution at the VBM (w_{O-2p}) for (b) 845 target oxides and (c) 152 oxides remaining after screening.

Since oxygen vacancies are major “hole killers,” screening oxides by their formation energies efficiently filters out unsuitable oxides. The targets are the same 845 oxides as those in Ref.,³⁴ which satisfy the following criteria: (i) stable against competing phases, (ii) band gaps are larger than 0.3 eV in the Materials Project Database (MPD), (iii) nonmagnetic, and (iv) the number of atoms in their primitive cells is 30 or less in the MPD (See Method for details). To avoid complex systems comprising mixed anions and/or cations with spin-

polarized d or f orbitals, oxides containing H, He, C–Ne, P–Ar, Mn–Ni, Se–Kr, Tc–Rh, Te–Xe, Pr–Lu, Os, Ir, and Po–Lr were excluded. Note that SnO is not included in our targets since it is unstable with respect to SnO₂ and O₂.

When a sufficient number of holes are introduced, the Fermi level is positioned near the VBM. For example, in ZnO, when the hole concentration is 10^{17} cm⁻³, the Fermi level lies at 0.2 eV at 300 K (see the Supporting Information). Therefore, to prevent hole compensation by oxygen vacancies, all inequivalent oxygen vacancies must be stable near the VBM, either (i) in neutral charge states or (ii) in positive charge states with positive formation energies. In this study, we considered the O-rich conditions to suppress oxygen vacancies as much as possible (see Method).

Consequently, only 152 out of the 845 oxides satisfy this criterion. They are primarily composed of group 10 and 11 elements (Pd, Pt, Cu, Ag, Au) (Fig. 2(a)), which tend to possess fully occupied d orbitals. In contrast, oxides containing early transition-metal cations (e.g., Sc, Y, Ti, V, Nb) are relatively scarce, mainly because their unoccupied d states do not typically contribute to raising the O-2 p manifold. Oxides containing alkali and alkaline earth metals remain relatively abundant, as they are components of ternary or quaternary oxides.

O-2 p orbital contributions at valence band maxima

To identify oxides whose VBM mainly consists of O-2 p orbitals, we computed the projected values of the VBM wavefunctions onto the O-2 p orbitals ($w_{\text{O-2}p}$) for 845 oxides (see Method). As shown in Fig. 2 (b), most oxides exhibit substantial $w_{\text{O-2}p}$, typically above 0.6. After screening based on the oxygen vacancy formation energies, the average $w_{\text{O-2}p}$ value decreases from 0.63 (Fig. 2(b)) to 0.40 (Fig. 2(c)). This highlights that oxides whose VBMs are mainly composed of O-2 p orbitals are largely excluded.

Figure 3 shows $w_{\text{O-2}p}$ and the corresponding names of oxides, sorted in descending order of $w_{\text{O-2}p}$. Here, we classify oxides into four categories. The first category includes oxides with

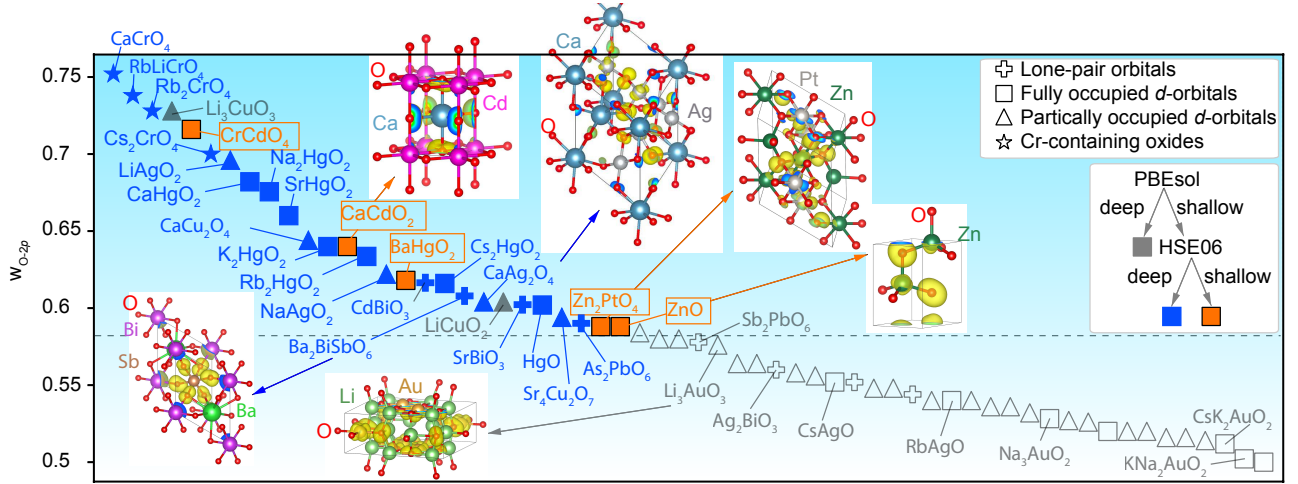


Figure 3: The O-2p contributions at the VBM (w_{O-2p}) are shown in descending order. Oxides are categorized into four classes, as indicated in the legend (see text for details). For oxides with w_{O-2p} greater than that of ZnO, the acceptor levels introduced by dopants are also classified into three categories. Gray symbols indicate oxides with deep acceptor levels in PBEsol calculations. Blue symbols represent oxides that have shallow acceptor levels in PBEsol but become deep in HSE06. Orange symbols denote oxides with shallow acceptor levels even when using HSE06. Isosurface plots of representative oxides are shown at 5% of the maximum electron density.

lone-pair orbitals near the VBM, namely Pb^{2+} and Bi^{3+} . The second and third categories consist of oxides with fully or partially occupied d electrons in or near the valence bands, respectively. In the former case, the oxides include Ag^+ , Au^+ , Zn^{2+} , Cd^{2+} , and Hg^{2+} , whereas in the latter case, they include Cu^{3+} , Ag^{3+} , Pt^{4+} , and Pd^{4+} . The remaining compounds include Cr-containing oxides, namely $CaCrO_4$, $RbLiCrO_4$, Rb_2CrO_4 , and Cs_2CrO_4 . When an oxide falls into more than one category, it is assigned to the earliest applicable category. Such oxides are $CrCdO_4$, Ag_2BiO_3 , $CdBiO_3$, $CdAuO_2$ (Au^+ and Au^{3+}), and $Rb_5Au_3O_2$ (Au^-), the last two of which are classified as oxides with fully occupied d electrons. All the Cr-containing oxides exhibit significantly high w_{O-2p} , indicating a lower contribution of unoccupied Cr-3d orbitals to the VBM. A detailed electronic structures of Cr-containing oxides are discussed later.

In Figure 3, we show isosurfaces of squared wavefunctions at the VBM in representative oxides (see Method). These illustrate how w_{O-2p} relates to the spatial distributions of the

VBM. Oxides in the middle-to-lower region of Figure 3 tend to exhibit hybridization of O-2*p* orbitals with other orbitals. For example, the O-2*p* orbitals in ZnO are slightly hybridized with the deep Zn-3*d* orbitals. Ba₂BiSbO₆ and CaAg₂O₄ also show contributions from Bi lone pairs and Ag-4*d* orbitals, respectively. On the other hand, CaCdO₂, which exhibits a higher $w_{\text{O-2}p}$ of 0.64, shows only O-2*p* character. However, it should be noted that a higher $w_{\text{O-2}p}$ does not always correspond to a dominant O-2*p* character at the VBM, as exemplified by Ba₂BiSbO₆, where the presence of Bi lone-pair orbitals is evident. This indicates that analyzing the VBM character using $w_{\text{O-2}p}$ is qualitative. Thus, we applied a looser criterion by retaining oxides with $w_{\text{O-2}p}$ greater than that of ZnO (0.588) to avoid false negatives; As a result, 27 out of 152 oxides remained. We also manually excluded CdBiO₃, SrBiO₃, As₂PbO₅, and Ba₂BiSbO₆ because they exhibit lone-pair orbital characteristics as exemplified by Ba₂BiSbO₆ in Figure 3 and the Supporting Information. Consequently, 23 oxides were retained for further analysis. Note that CuAlO₂ ($w_{\text{O-2}p}$ =0.128) and the well-known *p*-type B₆O³⁶ ($w_{\text{O-2}p}$ =0.118) are excluded at this step, since their VBMs are mainly composed of Cu-3*d* and B-2*p* orbitals,³⁷ respectively. Some representative *p*-type TCOs that satisfy the “VBM-raising strategy” are listed in the Table S4 in the Supporting Information, together with the steps where they are excluded from our screening. This supports the validity of our screening.

Acceptor doping

When synthesizing *p*-type semiconductors, the presence of dopants that exhibit shallow acceptor levels is crucial. Therefore, in the next step, we calculated the acceptor dopants in the remaining 23 oxides. In this study, we considered acceptor-type dopants substituting at cationic sites, as this type of doping can be readily achieved by simply sintering the host oxide together with a dopant-containing oxide during synthesis. We selected representative acceptors: Na for divalent, Ca for trivalent, Sc for tetravalent, Si for pentavalent, and V for hexavalent cations. The detailed information is presented in the Supporting Information.

Note that, with this approach, oxides composed solely of monovalent cations are not hole-dopable, since it is generally uncommon to dope closed-shell noble gas elements. Fortunately, none of the remaining 23 oxides fall into this category.

As shown in Figure 3, most oxides (21 out of 23) are predicted to exhibit shallow acceptor levels based on PBEsol calculations. This number is, however, significantly reduced when using the more accurate HSE06 hybrid functional, which provides improved band gap estimations, leaving only six oxides: CrCdO_4 , CaCdO_2 , CaCu_2O_4 , BaHgO_2 , Zn_2PtO_4 , and ZnO . This result indicates that employing more accurate functionals than PBEsol is crucial for reliably identifying hole-dopability in oxides. Unfortunately, although Cr-containing oxides exhibit higher $w_{\text{O-}2p}$, all of them exhibit deep acceptor levels except for CrCdO_4 (see the Supporting Information).

Electronic band structures, densities of states (DOS), and squared wavefunctions at the VBM for the remaining six oxides are shown in Figure 4(a-f). They confirm that the O-2*p* orbitals predominantly compose the valence bands in all these compounds. However, all of them exhibit fully occupied *d* semi-core states between -8 and -5 eV relative to each VBM, which are expected to slightly hybridize with the O-2*p* orbitals, tending to elevate the VBM. Indeed, the squared wavefunctions of BaHgO_2 , ZnO , Zn_2PtO_4 , and CaCu_2O_4 reveal the presence of Cu-3*d*, Zn-3*d*, or Hg-5*d* orbital components, despite their relatively high $w_{\text{O-}2p}$ values. Thus, we conclude that hole doping into the pure O-2*p* bands is nearly impossible, and at least such a small hybridization with the valence band is necessary to enable hole doping into the O-2*p* orbitals.

The electronic band structures and DOS for CaCrO_4 , RbLiCrO_4 , Rb_2CrO_4 , and Cs_2CrO_4 are shown in Figure S7 in the Supporting Information. Similar to CrCdO_4 , all of them exhibit valence bands dominated by O-2*p* states. Interestingly, RbLiCrO_4 , Rb_2CrO_4 , and Cs_2CrO_4 show very low valence band dispersion. This is primarily due to the low oxygen ion density in these oxides. Consequently, only CrCdO_4 , which is classified as a fully occupied *d*-electron oxide, shows higher hybridization of the VBM with the Cr-3*d* orbitals, and thus a shallow

acceptor level.

We emphasize that ZnO remains in our screening. Indeed, Tsukazaki *et al.* reported *p*-type ZnO using nitrogen as a *p*-type dopant,³⁸ demonstrating a light-emitting diode; however, hole doping in ZnO remains extremely challenging. See the recent review paper,³⁹ which outlines various stringent conditions for realizing *p*-type ZnO.

Defect formation energies in CrCdO₄ and CaCdO₂

Since CrCdO₄ and CaCdO₂ exhibit stronger O-2*p* character in Figure 4, it is of importance whether they can exhibit hole conductivity. To determine this, we need the total energies of all point defects that may compensate carrier holes and/or pin the Fermi level, as well as the acceptor dopants. We therefore performed their calculations using the HSE06 hybrid functional. We consider vacancies, cation antisites, and interstitials as native defects, and acceptor-type dopants substituted at cation or interstitial sites (see Methods).

CrCdO₄ crystallizes in the orthorhombic space group *Cmcm*. Experimental reports are very limited: its crystal structure was refined by Müller *et al.*,⁴⁰ and Bodade *et al.* measured the frequency-dependent dielectric constant of Sr-doped CrCdO₄.⁴¹ Based on our HSE06 calculations, CrCdO₄ exhibits relatively low hole effective masses of 1.35, 1.73, and 1.64 m_0 along the *x*-, *y*-, and *z*-directions, respectively (see the Supporting Information), where m_0 is the electron rest mass. These values indicate promising hole mobility. The calculated optical band gap is 3.48 eV, which suggests that it could serve as a *p*-type TCO if sufficient hole doping is achievable.

The formation energies of native defects under O-rich and Cd-poor conditions are shown in Fig. 5(a). Oxygen vacancies have positive formation energies even when the Fermi level is near the VBM, consistent with our initial screening. However, interstitials generally have lower formation energies, which significantly restricts the accessible Fermi level range. As a result, achieving a high hole concentration would be difficult.

The structure of CaCdO₂ registered in the MPD belongs to the space group *P4/mmm*, in

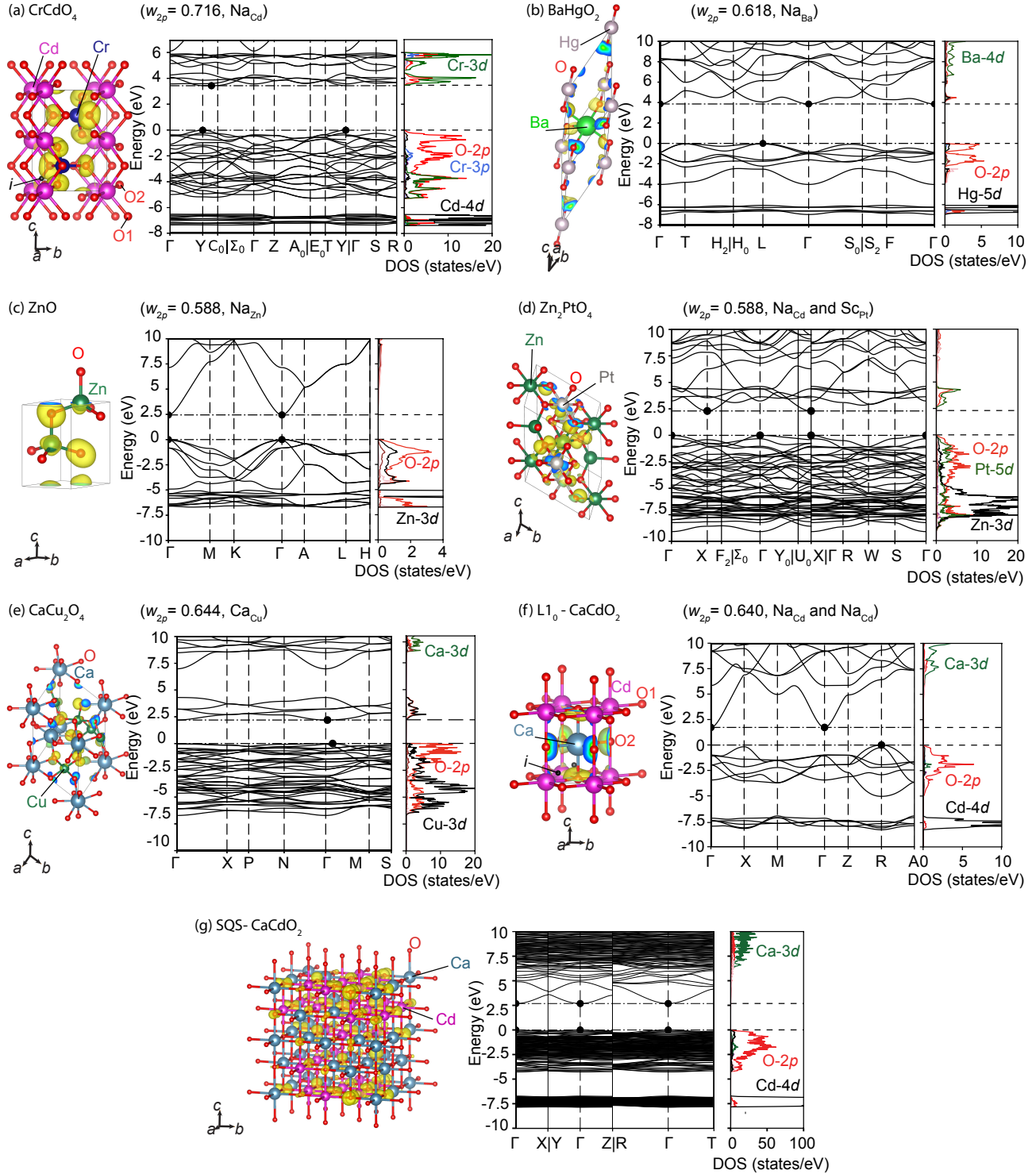


Figure 4: Crystal structures with squared wavefunctions at the VBM, electronic band structures, and densities of states for (a) CrCdO_4 , (b) BaHgO_2 , (c) ZnO , (d) Zn_2PtO_4 , (e) CaCu_2O_4 , and (f) $\text{L1}_0\text{-CaCdO}_2$, and (g) SQS model for CaCdO_2 . The O-2p contributions at the VBM ($w_{\text{O-2p}}$) and the dopants confirmed to behave as shallow acceptors are also indicated in parentheses.

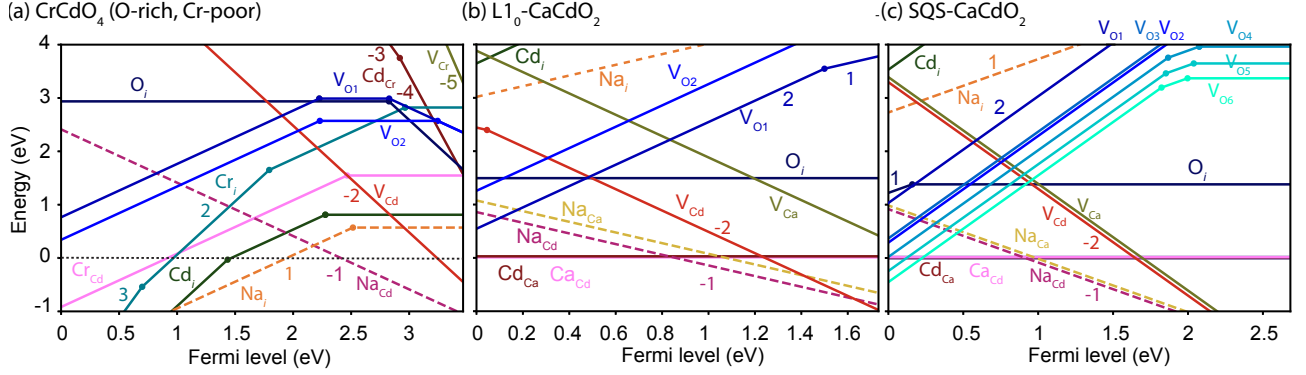


Figure 5: Formation energies of native defects (solid lines) and Na dopants (dashed lines) as a function of the Fermi level in (a) CrCdO_4 (O-rich, Cr-poor), (b) $\text{L1}_0\text{-CaCdO}_2$, and (c) SQS model for CaCdO_2 . The chemical potentials are set at oxygen-rich conditions (see the Supporting Information). V_X denotes a vacancy at the X site, while X_i denotes an interstitial at the X position. The atomic sites and interstitial sites are shown in the crystal structures in Figure 4. X_Y denotes an antisite defect where X is substituted at the Y site. In (c), only the lowest formation energies are shown for each defect type except for the oxygen vacancies.

which cations are arranged in the L1_0 -type layered configuration. However, CaCdO_2 is known to exhibit cation disorder experimentally, forming a cation disordered rock-salt structure with space group $Fm\bar{3}m$. This behavior can be rationalized by the identical oxidation states and similar ionic radii of Ca^{2+} (1.00 Å) and Cd^{2+} (0.95 Å) in sixfold coordination.⁴² Experimental data for CaCdO_2 are also scarce, with the notable exception of the study by Srihari et al.,⁴³ which reported how the lattice constant and band gap vary as a function of Ca fraction.

We modeled the disordered phase using the special quasi-random structure (SQS) technique⁴⁴ (see Method). The atomic arrangement, band structure, DOS, and squared wavefunction at the VBM of the SQS model are shown in Figure 4(g). The fundamental gap of the ordered model is 1.73 eV, while that for the SQS model is 2.68 eV. This large discrepancy is primarily due to the narrower dispersion of the conduction band in the SQS model; in both the ordered and SQS models, the conduction bands are composed of the Ca-3d orbitals, and their interactions are weaker in the SQS model due to the inhomogeneous bonding between Ca atoms. The optical gap of the SQS model is 3.30 eV, which is higher than the experimental value of 2.83 eV.⁴³ Since such an optical gap is nearly transparent, CaCdO_2 is

also expected to be a p -type TCO. The hole effective masses in the SQS model are about 1.8–1.9 m_0 , which is comparable to those in GaN ($1.40 \pm 0.33 m_0$).⁴⁵

Focusing on the point defects in the ordered CaCdO_2 (Fig. 5(b)), the oxygen vacancies again exhibit positive formation energies under the O-rich and p -type conditions, consistent with our screening. However, unlike CrCdO_4 , other donor-type defects such as cation interstitials exhibit higher formation energies, and do not introduce any pinning levels. This would be simply because the vacant space in the rock-salt structure is smaller than CrCdO_4 . In addition, Na dopants exhibit lower formation energies at the Cd sites (Na_{Cd}) and higher formation energies at the interstitial sites, which hinders the self-compensation of Na dopants. As anticipated from the disordering behavior, cation antisites exhibit very low formation energies, but they are stable in the neutral charge states and thus do not affect the carrier concentration. In CaO , oxygen interstitials exhibit amphoteric behavior and low formation energies, introducing deep pinning levels that prohibit a high concentration of hole doping.⁴⁶ However, this is not the case in CaCdO_2 , due to its higher VBM compared to CaO . Consequently, a high hole concentration can be introduced by Na dopants (see the Supporting Information).

Since experimental samples of CaCdO_2 are disordered, defect formation energies computed using the SQS model are particularly relevant. We investigated cation vacancies, cation antisites, and Na substitution at three randomly selected Ca and three Cd sites (see the Supporting Information), based on the fact that each cation site is coordinated by six nearest-neighbor oxygen atoms and the site dependence of formation energies is relatively small. In contrast, oxygen vacancies were analyzed according to the number of surrounding Cd atoms, since oxygen vacancy formation energies in CdO and CaO are nearly identical despite the VBM of CdO being 1.5 eV higher (see Fig. 6 shown later), suggesting weaker Cd–O bonding compared to Ca–O. Indeed, as Cd coordination increases, the formation energy of oxygen vacancies tends to decrease (see Fig. 5(c)). Interestingly, except for the oxygen vacancies, the formation energies of point defects in the ordered CaCdO_2 and SQS model are

almost the same when we assume the VBM positions are close to each other (see Fig. 5(b,c)).

Band alignment

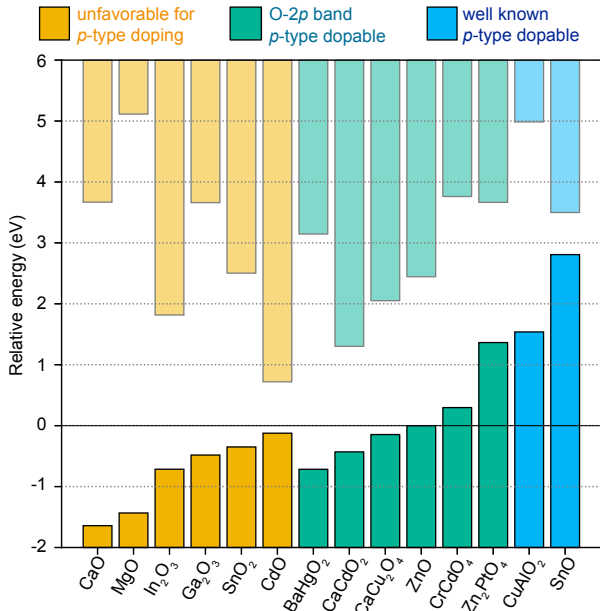


Figure 6: Band alignment obtained using HSE06, showing the VBM across three groups: (i) oxides unfavorable for p -type doping, (ii) oxides identified in this study as O-2 p band p -type dopable candidates, and (iii) well-known p -type dopable oxides. The energy zero is set to the VBM in ZnO.

Finally, we discuss hole dopability based on band alignment. Several references can be used for aligning band edges, such as the vacuum level estimated from slab models,⁴⁷ branch point energies (BPE),⁴⁸ and core potentials.^{49–51} We note that none of these methods is perfect. For example, using the vacuum level, the alignment depends on the surface orientation, while the BPE largely depends on the number of bands considered^{48,52} (see the Supporting Information). In this study, we constructed the band alignment using the O-2 p core potentials. The advantage of this approach is that it eliminates such arbitrariness; however, it is a bold assumption that the oxygen core potential remains constant across all oxides. For reference, we also present the band alignment based on the BPE in the Supporting Information.

Figure 6 presents the band alignment obtained from HSE06 calculations for: (i) oxides unfavorable for p -type doping; (ii) oxides identified in this study as hole-dopable candidates into the O-2 p orbitals by cationic acceptor dopants; and (iii) CuAlO₂ and SnO, which satisfy the “VBM-raising strategy.” CuAlO₂ and SnO, well-known p -type TCOs, exhibit significantly higher VBMs, and Zn₂PtO₄ and CrCdO₄ also show relatively higher VBM compared to hole undopable oxides. However, the hole dopability into O-2 p orbitals appears difficult to predict only from the alignment, as illustrated by the comparison between CaCdO₂ and CdO. One of the primary reasons is that the band alignment does not include information on defect formation energies, which depend on the controllability of the chemical potential. Previous studies have used band alignment to screen materials for dopability.^{52–54} However, based on our results, caution is needed to avoid screening out many false negatives.

Conclusions

In this work, we systematically screened 845 oxides to identify those in which holes can be introduced into the VBM composed of O-2 p orbitals. Our results underscore the intrinsic challenge of hole doping in these systems, with only CaCdO₂ emerging from the screening. Notably, its VBM is hybridized with deep-lying Cd-3 d orbitals. This highlights that, without cation d orbitals or lone-pair bands, hole doping into a pure O-2 p band is extremely difficult, if not impossible. Thus, our research reinforces the effectiveness of the “VBM-raising strategy.” We also investigated whether hole dopability can be simply predicted from the band alignment, and found that while a high VBM is related to hole dopability, it is insufficient alone, as dopability is also influenced by other factors such as the controllability of the chemical potential.

Methods

Computational setting of first-principles calculations

First-principles calculations were performed using the projector augmented-wave (PAW) method,^{55,56} as implemented in VASP.⁵⁷ Details of the PAW potentials are provided in Ref.^{34,35} In this study, we used the PBEsol exchange-correlation functional⁵⁸ and the standard HSE06 hybrid functional.⁵⁹ Effective mass tensors were computed using BoltzTraP2,⁶⁰ assuming a typical carrier concentration of 10^{18} cm⁻³ and a temperature of 300 K. For the optical absorption spectra, the real parts of the dielectric functions were obtained from the imaginary parts via the Kramers–Kronig transformation, using a complex shift of 0.01 eV.⁶⁰ The optical band gaps were then defined from the Tauc plots (see the Supporting Information). Band paths for electronic structure calculations were generated automatically using SeeK-path.⁶¹ The values of the VBM wavefunctions projected onto the O-2*p* orbitals ($w_{\text{O-2}p}$) were calculated using the oxygen PAW core radius of 0.804 Å. We constructed the band alignment using oxygen core potentials as a reference. When there are multiple O sites, we used the averaged value. Crystal structures and isosurface plots were generated using VESTA.⁶² We constructed the 64-atom SQS model using the ATAT code.⁶³ Starting from a $2 \times 2 \times 2$ conventional rock-salt structure, we included clusters up to quadruplets and interactions up to the second-nearest neighbors. All VASP input files were generated using VISE,³⁵ and defect models were constructed and analyzed with pydefect.³⁵ More details, such as parameter settings, are described in the Supporting Information.

Target oxides

Since we utilize the previously calculated oxygen vacancy formation energy database, we used the same 845 target oxides as in Ref.³⁴ The target oxides were retrieved on May 14, 2021, from the Materials Project Database (MPD).⁶⁴ Note that their stability was determined based on the PBE(+U) calculations at that time.⁶²

Modeling of point defects

Defect calculations were carried out using supercells containing 192 atoms for CrCdO_4 , and 64 atoms for both ordered and disordered CaCdO_2 (see the Supporting Information). The supercells used for calculating the acceptor dopants in the other oxides are described in the Supporting Information. The internal atomic positions were relaxed while keeping the lattice constants fixed at their theoretical values. All defect calculations allowed spin polarization. The interstitial sites were determined from the local minima of the electron charge density, as shown in Fig. 4 (a) and (f). The oxygen interstitial sites in CaCdO_2 are found to be stable in split-type O_2 dimers, as plotted in Figure S9(b) and S10(d) in the Supporting Information. In Section Acceptor doping, we validated the shallow acceptor behavior from single-particle levels (see the Supporting Information). The carrier concentrations as a function of the Fermi level were calculated from the DOS via the Fermi-Dirac distribution.⁶⁵ The defect concentrations were estimated from the Boltzmann distribution, considering the site degeneracies that depend on the defect site symmetries in the relaxed structures and the spin degeneracies,⁶⁵ and shown in Figure S2 in the Supporting Information. The synthesis temperatures for each candidate were set based on the conditions reported in previous experiments.^{38,39,41,43,66,67}

The finite-size effects on the formation energies of charged defects were corrected using the extended FNV method.^{65,68,69} Static dielectric tensors (ϵ_0) were obtained as the sum of the high-frequency ion-clamped dielectric tensor (ϵ_∞) and the ionic contribution (ϵ_{ion}), calculated using density functional perturbation theory.⁷⁰⁻⁷² ϵ_∞ were derived from HSE06 calculations, while ϵ_{ion} were computed using PBEsol to reduce computational cost. Local field effects were included in the evaluation of ϵ_∞ . Dielectric constants of the SQS model were approximated by taking the average of those in CdO and CaO, since their calculations are computationally too demanding. Chemical potential diagrams (CPDs) were constructed using the total energies calculated using HSE06 at 0 K. The energy difference between the ordered and disordered structures of CaCdO_2 is only 0.3 meV/atom. Since they are slightly unstable with respect to competing phases, we decreased their total energies by only 5 meV/atom so that they appear

in the CPD. Candidate competing phases were obtained from the Materials Project.⁶⁴ A full list of competing phases used is provided in the Supporting Information.

Acknowledgement

This work has been supported by JST FOREST Program (JPMJFR235S), and KAKENHI (22H01755 and 25K01486).

Supporting Information Available

The Supporting Information is available free of charge at [TO BE INSERTED].

References

- (1) Nomura, K.; Ohta, H.; Takagi, A.; Kamiya, T.; Hirano, M.; Hosono, H. Room-temperature fabrication of transparent flexible thin-film transistors using amorphous oxide semiconductors. *Nature* **2004**, *432*, 488–492.
- (2) Pal, S.; Basak, D. Ultrathin Oxide/Metal/Oxide Trilayer Transparent Conducting Electrodes for an All-Transparent Flexible UV Photodetecting Device. *ACS Applied Electronic Materials* **2024**, *6*, 7035–7045.
- (3) Higashiwaki, M.; Sasaki, K.; Murakami, H.; Kumagai, Y.; Koukitu, A.; Kuramata, A.; Masui, T.; Yamakoshi, S. Recent progress in Ga₂O₃ power devices. *Semiconductor Science and Technology* **2016**, *31*, 034001.
- (4) Baker, L. R.; Diebold, U.; Park, J. Y.; Selloni, A. Oxide chemistry and catalysis. *The Journal of Chemical Physics* **2020**, *153*, 050401.
- (5) Krishnan, A.; Swarnalal, A.; Das, D.; Krishnan, M.; Saji, V. S.; Shibli, S. A review

- on transition metal oxides based photocatalysts for degradation of synthetic organic pollutants. *Journal of Environmental Sciences* **2024**, *139*, 389–417.
- (6) Zhu, Y.; He, Y.; Jiang, S.; Zhu, L.; Chen, C.; Wan, Q. Indium–gallium–zinc–oxide thin-film transistors: Materials, devices, and applications. *Journal of Semiconductors* **2021**, *42*, 031101.
- (7) Sharma, D. K.; Shukla, S.; Sharma, K. K.; Kumar, V. A review on ZnO: Fundamental properties and applications. *Materials Today: Proceedings* **2022**, *49*, 3028–3035, National Conference on Functional Materials: Emerging Technologies and Applications in Materials Science.
- (8) Jo, G.; Hong, W.-K.; Maeng, J.; Kim, T.-W.; Wang, G.; Yoon, A.; Kwon, S.-S.; Song, S.; Lee, T. Structural and electrical characterization of intrinsic *n*-type In₂O₃ nanowires. *Colloids and Surfaces A: Physicochemical and Engineering Aspects* **2008**, *313-314*, 308–311, Nanoscience and Nanotechnology.
- (9) Rauf, I. A. Structure and properties of tin-doped indium oxide thin films prepared by reactive electron-beam evaporation with a zone-confining arrangement. *Journal of Applied Physics* **1996**, *79*, 4057–4065.
- (10) Zhang, K. H. L.; Xi, K.; Blamire, M. G.; Egdell, R. G. *P*-type transparent conducting oxides. *Journal of Physics: Condensed Matter* **2016**, *28*, 383002.
- (11) Hu, L.; Wei, R. H.; Tang, X. W.; Lu, W. J.; Zhu, X. B.; Sun, Y. P. Design strategy for *p*-type transparent conducting oxides. *Journal of Applied Physics* **2020**, *128*, 140902.
- (12) Willis, J.; Scanlon, D. O. Latest directions in *p*-type transparent conductor design. *J. Mater. Chem. C* **2021**, *9*, 11995–12009.
- (13) Gunkel, F.; Christensen, D. V.; Chen, Y. Z.; Pryds, N. Oxygen vacancies: The (in)visible friend of oxide electronics. *Applied Physics Letters* **2020**, *116*, 120505.

- (14) Cao, R.; Deng, H.-X.; Luo, J.-W. Design Principles of p -Type Transparent Conductive Materials. *ACS Applied Materials & Interfaces* **2019**, *11*, 24837–24849, PMID: 30995003.
- (15) Hautier, G.; Miglio, A.; Ceder, G.; Rignanese, G.-M.; Gonze, X. Identification and design principles of low hole effective mass p -type transparent conducting oxides. *Nat. Commun.* **2013**, *4*, 2292.
- (16) Kawazoe, H.; Yasukawa, M.; Hyodo, H.; Kurita, M.; Yanagi, H.; Hosono, H. P -type electrical conduction in transparent thin films of CuAlO_2 . *Nature* **1997**, *389*, 939–942.
- (17) Sheng, S.; Fang, G.; Li, C.; Xu, S.; Zhao, X. p -type transparent conducting oxides. *physica status solidi (a)* **2006**, *203*, 1891–1900.
- (18) Gake, T.; Kumagai, Y.; Takahashi, A.; Oba, F. Point defects in p -type transparent conductive CuMO_2 ($M = \text{Al, Ga, In}$) from first principles. *Phys. Rev. Mater.* **2021**, *5*, 104602.
- (19) Ueda, K.; Hase, T.; Yanagi, H.; Kawazoe, H.; Hosono, H.; Ohta, H.; Orita, M.; Hirano, M. Epitaxial growth of transparent p -type conducting CuGaO_2 thin films on sapphire (001) substrates by pulsed laser deposition. *J. Appl. Phys.* **2001**, *89*, 1790–1793.
- (20) Zhang, N.; Sun, J.; Gong, H. Transparent p -Type Semiconductors: Copper-Based Oxides and Oxychalcogenides. *Coatings* **2019**, *9*.
- (21) Varley, J. B.; Schleife, A.; Janotti, A.; Van de Walle, C. G. Ambipolar doping in SnO . *Appl. Phys. Lett.* **2013**, *103*, 082118.
- (22) Walsh, A.; Payne, D. J.; Egdell, R. G.; Watson, G. W. Stereochemistry of post-transition metal oxides: revision of the classical lone pair model. *Chem. Soc. Rev.* **2011**, *40*, 4455–4463.

- (23) Shi, J.; Rubinstein, E. A.; Li, W.; Zhang, J.; Yang, Y.; Lee, T.-L.; Qin, C.; Yan, P.; MacManus-Driscoll, J. L.; Scanlon, D. O.; Zhang, K. H. Modulation of the Bi³⁺ 6s² Lone Pair State in Perovskites for High-Mobility p-Type Oxide Semiconductors. *Advanced Science* **2022**, *9*, 2104141.
- (24) Huyen, V. T. N.; Bae, S.; Costa-Amaral, R.; Kumagai, Y. Native defects and p-type dopability in transparent β -TeO₂: A first-principles study. *Phys. Rev. Appl.* **2024**, *22*, 044065.
- (25) Chen, H.; Harding, J. H. Nature of the hole states in Li-doped NiO. *Phys. Rev. B* **2012**, *85*, 115127.
- (26) Molaei, R.; Bayati, R.; Narayan, J. Crystallographic Characteristics and p-Type to n-Type Transition in Epitaxial NiO Thin Film. *Cryst. Growth Des.* **2013**, *13*, 5459–5465.
- (27) Arca, E.; Kehoe, A. B.; Veal, T. D.; Shmeliov, A.; Scanlon, D. O.; Downing, C.; Daly, D.; Mullarkey, D.; Shvets, I. V.; Nicolosi, V.; Watson, G. W. Valence band modification of Cr₂O₃ by Ni-doping: creating a high figure of merit p-type TCO. *J. Mater. Chem. C* **2017**, *5*, 12610–12618.
- (28) Jellite, M.; Rehspringer, J.-L.; Fazio, M.; Muller, D.; Schmerber, G.; Ferblantier, G.; Colis, S.; Dinia, A.; Sugiyama, M.; Slaoui, A.; Cavalcoli, D.; Fix, T. Investigation of LaVO₃ based compounds as a photovoltaic absorber. *Solar Energy* **2018**, *162*, 1–7.
- (29) Ainabayev, A.; Walls, B.; Mullarkey, D.; Caffrey, D.; Fleischer, K.; Smith, C. M.; McGlinchey, A.; Casey, D.; McCormack, S. J.; Shvets, I. High-performance p-type V₂O₃ films by spray pyrolysis for transparent conducting oxide applications. *Scientific Reports* **2024**, *14*, 1928.
- (30) Liu, K.; Wei, J.; Meng, L.; Han, D.; Chen, L.; Liu, N.; Hu, S.; Ji, L.; Cui, P.; Zhang, W.; Ye, J. Activating p-type conduction and visible transparency in delafossite CuAlO₂

- films: The critical role of the copper valence state transition. *Materials Today Physics* **2024**, *40*, 101304.
- (31) Caraveo-Frescas, J. A.; Nayak, P. K.; Al-Jawhari, H. A.; Granato, D. B.; Schwingenschlögl, U.; Alshareef, H. N. Record Mobility in Transparent *p*-Type Tin Monoxide Films and Devices by Phase Engineering. *ACS Nano* **2013**, *7*, 5160–5167.
- (32) K., A. Electric field dependence of the electron mobility in bulk wurtzite ZnO. *Bulletin of Materials Science* **2014**, *37*, 1603–1606.
- (33) Galazka, Z.; Uecker, R.; Klimm, D.; Irmscher, K.; Pietsch, M.; Schewski, R.; Albrecht, M.; Kwasniewski, A.; Ganschow, S.; Schulz, D.; Guguschev, C.; Bertram, R.; Bickermann, M.; Fornari, R. Growth, characterization, and properties of bulk SnO₂ single crystals. *physica status solidi (a)* **2014**, *211*, 66–73.
- (34) Kumagai, Y. Computational Screening of *p*-Type Transparent Conducting Oxides Using the Optical Absorption Spectra and Oxygen-Vacancy Formation Energies. *Phys. Rev. Appl.* **2023**, *19*, 034063.
- (35) Kumagai, Y.; Tsunoda, N.; Takahashi, A.; Oba, F. Insights into oxygen vacancies from high-throughput first-principles calculations. *Phys. Rev. Mater.* **2021**, *5*, 123803.
- (36) Akashi, T.; Itoh, T.; Gunjishima, I.; Masumoto, H.; Goto, T. Thermoelectric Properties of Hot-pressed Boron Suboxide (B₆O). *Materials transactions* **2002**, *43*, 1719–1723.
- (37) Varley, J. B.; Lordi, V.; Miglio, A.; Hautier, G. Electronic structure and defect properties of B₆O from hybrid functional and many-body perturbation theory calculations: A possible ambipolar transparent conductor. *Phys. Rev. B* **2014**, *90*, 045205.
- (38) Tsukazaki, A.; Ohtomo, A.; Onuma, T.; Ohtani, M.; Makino, T.; Sumiya, M.; Ohtani, K.; Chichibu, S. F.; Fuke, S.; Segawa, Y.; Ohno, H.; Koinuma, H.; Kawasaki, M.

- Repeated temperature modulation epitaxy for *p*-type doping and light-emitting diode based on ZnO. *Nature Materials* **2005**, *4*, 42–46.
- (39) Yang, R.; Wang, F.; Lu, J.; Lu, Y.; Lu, B.; Li, S.; Ye, Z. ZnO with *p*-Type Doping: Recent Approaches and Applications. *ACS Applied Electronic Materials* **2023**, *5*, 4014–4034.
- (40) Müller, O.; White, W. B.; Roy, R. X-ray diffraction study of the chromates of nickel, magnesium and cadmium. *Zeitschrift für Kristallographie – Crystalline Materials* **1969**, *130*, 112–120.
- (41) Bodade, A. B.; Deshmukh, P. R.; Taiwade, M. A.; Chaudhari, G. N. AC impedance studies on strontium doped CdCrO₄ nanoparticles prepared by Sol-gel Citrate Method. *International Journal for Research Development in Technology* **2015**, *4*, 1–6.
- (42) Shannon, R. D. Revised effective ionic radii and systematic studies of interatomic distances in halides and chalcogenides. *Acta Crystallogr. Sect. A* **1976**, *32*, 751–767.
- (43) Srihari, V.; Sridharan, V.; Chandra, S.; Sastry, V. S.; Sahu, H. K.; Sundar, C. S. Wide band gap tunability of bulk Cd_{1-x}Ca_xO. *Journal of Applied Physics* **2011**, *109*, 013510.
- (44) van de Walle, A.; Tiwary, P.; de Jong, M.; Olmsted, D.; Asta, M.; Dick, A.; Shin, D.; Wang, Y.; Chen, L.-Q.; Liu, Z.-K. Efficient stochastic generation of special quasirandom structures. *Calphad* **2013**, *42*, 13–18.
- (45) Kasic, A.; Schubert, M.; Einfeldt, S.; Hommel, D.; Tiwald, T. E. Free-carrier and phonon properties of *n*- and *p*-type hexagonal GaN films measured by infrared ellipsometry. *Phys. Rev. B* **2000**, *62*, 7365–7377.
- (46) Yuan, Z.; Hautier, G. First-principles study of defects and doping limits in CaO. *Applied Physics Letters* **2024**, *124*, 232101.

- (47) Kumagai, Y.; Butler, K. T.; Walsh, A.; Oba, F. Theory of ionization potentials of nonmetallic solids. *Phys. Rev. B* **2017**, *95*, 125309.
- (48) Schleife, A.; Fuchs, F.; Rödl, C.; Furthmüller, J.; Bechstedt, F. Branch-point energies and band discontinuities of III-nitrides and III-/II-oxides from quasiparticle band-structure calculations. *Applied Physics Letters* **2009**, *94*, 012104.
- (49) Kraut, E. A.; Grant, R. W.; Waldrop, J. R.; Kowalczyk, S. P. Precise Determination of the Valence-Band Edge in X-Ray Photoemission Spectra: Application to Measurement of Semiconductor Interface Potentials. *Phys. Rev. Lett.* **1980**, *44*, 1620–1623.
- (50) Kraut, E. A.; Grant, R. W.; Waldrop, J. R.; Kowalczyk, S. P. Semiconductor core-level to valence-band maximum binding-energy differences: Precise determination by x-ray photoelectron spectroscopy. *Phys. Rev. B* **1983**, *28*, 1965–1977.
- (51) Yu, E. T.; Croke, E. T.; Chow, D. H.; Collins, D. A.; Phillips, M. C.; McGill, T. C.; McCaldin, J. O.; Miles, R. H. Measurement of the valence band offset in novel heterojunction systems: Si/Ge (100) and AlSb/ZnTe (100). *Journal of Vacuum Science and Technology B: Microelectronics Processing and Phenomena* **1990**, *8*, 908–915.
- (52) Woods-Robinson, R.; Broberg, D.; Faghaninia, A.; Jain, A.; Dwaraknath, S. S.; Persson, K. A. Assessing High-Throughput Descriptors for Prediction of Transparent Conductors. *Chemistry of Materials* **2018**, *30*, 8375–8389.
- (53) Garrity, E. M.; Lee, C.-W.; Gorai, P.; Tellekamp, M. B.; Zakutayev, A.; Stevanović, V. Computational Identification of Ternary Wide-Band-Gap Oxides for High-Power Electronics. *PRX Energy* **2022**, *1*, 033006.
- (54) Yim, K.; Youn, Y.; Lee, M.; Yoo, D.; Lee, J.; Cho, S. H.; Han, S. Computational discovery of *p*-type transparent oxide semiconductors using hydrogen descriptor. *npj Computational Materials* **2018**, *4*, 17.

- (55) Blöchl, P. E. Projector augmented-wave method. *Phys. Rev. B* **1994**, *50*, 17953–17979.
- (56) Kresse, G.; Joubert, D. From ultrasoft pseudopotentials to the projector augmented-wave method. *Phys. Rev. B* **1999**, *59*, 1758–1775.
- (57) Kresse, G.; Furthmüller, J. Efficient iterative schemes for *ab initio* total-energy calculations using a plane-wave basis set. *Phys. Rev. B* **1996**, *54*, 11169–11186.
- (58) Schimka, L.; Harl, J.; Kresse, G. Improved hybrid functional for solids: The HSEsol functional. *J. Chem. Phys.* **2011**, *134*, 024116.
- (59) Krukau, A. V.; Vydrov, O. A.; Izmaylov, A. F.; Scuseria, G. E. Influence of the exchange screening parameter on the performance of screened hybrid functionals. *J. Chem. Phys.* **2006**, *125*, 224106.
- (60) Madsen, G. K.; Carrete, J.; Verstraete, M. J. BoltzTraP2, a program for interpolating band structures and calculating semi-classical transport coefficients. *Comput. Phys. Commun.* **2018**, *231*, 140–145.
- (61) Hinuma, Y.; Pizzi, G.; Kumagai, Y.; Oba, F.; Tanaka, I. Band structure diagram paths based on crystallography. *Comput. Mater. Sci.* **2017**, *128*, 140–184.
- (62) Momma, K.; Izumi, F. *VESTA3* for three-dimensional visualization of crystal, volumetric and morphology data. *J. Appl. Crystallogr.* **2011**, *44*, 1272–1276.
- (63) van de Walle, A. Multicomponent multisublattice alloys, nonconfigurational entropy and other additions to the Alloy Theoretic Automated Toolkit. *Calphad* **2009**, *33*, 266–278, Tools for Computational Thermodynamics.
- (64) Jain, A.; Ong, S. P.; Hautier, G.; Chen, W.; Richards, W. D.; Dacek, S.; Cholia, S.; Gunter, D.; Skinner, D.; Ceder, G.; Persson, K. A. Commentary: The Materials Project: A materials genome approach to accelerating materials innovation. *APL Materials* **2013**, *1*, 011002.

- (65) Kumagai, Y.; Choi, M.; Nose, Y.; Oba, F. First-principles study of point defects in chalcopyrite ZnSnP_2 . *Phys. Rev. B* **2014**, *90*, 125202.
- (66) Thaowankaew, S.; Chao-moo, W.; Nontra-udorn, R.; Vora-ud, A.; Muthitamongkol, P.; Thanachayanont, C.; Seetawan, T. Preparation and thermopower of CaCuO_2 thin film. *Materials Today: Proceedings* **2018**, *5*, 14172–14176, The 4th Southeast Asia Conference on Thermoelectric, 15-18 December 2016.
- (67) Mikhailova, D.; Alyoshin, V.; Antipov, E.; Karpinski, J. Thermogravimetric Study of MHgO_2 ($M=\text{Ca, Sr, Ba}$) under Controlled Oxygen and Mercury Partial Pressures and Related Thermodynamics. *Journal of Solid State Chemistry* **1999**, *146*, 151–156.
- (68) Freysoldt, C.; Neugebauer, J.; Van de Walle, C. G. Fully *Ab initio* Finite-Size Corrections for Charged-Defect Supercell Calculations. *Phys. Rev. Lett.* **2009**, *102*, 016402.
- (69) Kumagai, Y.; Oba, F. Electrostatics-based finite-size corrections for first-principles point defect calculations. *Phys. Rev. B* **2014**, *89*, 195205.
- (70) Baroni, S.; Resta, R. *Ab initio* calculation of the macroscopic dielectric constant in silicon. *Phys. Rev. B* **1986**, *33*, 7017–7021.
- (71) Gajdoš, M.; Hummer, K.; Kresse, G.; Furthmüller, J.; Bechstedt, F. Linear optical properties in the projector-augmented wave methodology. *Phys. Rev. B* **2006**, *73*, 045112.
- (72) Nunes, R. W.; Gonze, X. Berry-phase treatment of the homogeneous electric field perturbation in insulators. *Phys. Rev. B* **2001**, *63*, 155107.

Supporting Information: Can the Oxygen $2p$ Band Be Hole Doped?

Thi Ngoc Huyen Vu[†] and Yu Kumagai^{*,†,‡}

[†]*Institute for Materials Research, Tohoku University, Sendai, Miyagi 980-8577, Japan*

[‡]*Division for the Establishment of Frontier Sciences, Organization for Advanced Studies,
Tohoku University, Sendai, Miyagi 980-8577, Japan*

E-mail: yukumagai@tohoku.ac.jp

Table S1: List of 27 oxides with w_{O-2p} higher than that of ZnO (0.588), screened as candidates for p -type oxides in this study, based on oxygen vacancy formation energies. Their Materials Project ID (MP-ID), space group, w_{O-2p} , category as defined in this study (see main text), acceptor dopants considered, and the number of atoms in the supercell for defect calculations (N_{atoms}) are also shown. The categories that contain "Partially (Full) occupied d -orbitals" are abbreviated as "Partially (Full)" for simplicity. **Bolded** doping defects indicate those that survived as shallow acceptors under HSE06. Since CdBiO_3 , SrBiO_3 , As_2PbO_5 , and $\text{Ba}_2\text{BiSbO}_6$ exhibit lone-pair orbital characteristics, their dopant calculations were not performed. Oxides containing only monovalent cations and lone-pair electrons are excluded (see text).

MP-ID	Formula	Space group	w_{O-2p}	Categories	Doping	N_{atoms}
mp-19215	CaCrO_4	$I4_1/amd$	0.752	Cr-based	Na_{Ca} , V_{Cr}	192
mp-18741	RbLiCrO_4	$P3_1c$	0.738	Cr-based	V_{Cr}	112
mp-17071	Rb_2CrO_4	$Pnma$	0.728	Cr-based	V_{Cr}	56
mp-19970	Li_3CuO_3	$P4_2/mnm$	0.728	Partially	Ca_{Cu}	234
mp-18781	CrCdO_4	$Cmcm$	0.716	Fully	Na_{Cd} , V_{Cr}	192
mp-647813	Cs_2CrO_4	$Pnma$	0.700	Cr-based	V_{Cr}	224
mp-996962	LiAgO_2	$P2_1/c$	0.696	Partially	Ca_{Ag}	288
mp-7041	CaHgO_2	$R\bar{3}m$	0.682	Fully	Na_{Hg} , Na_{Ca}	300
mp-4961	Na_2HgO_2	$I4/mmm$	0.676	Fully	Na_{Hg}	160
mp-665922	SrHgO_2	$R\bar{3}m$	0.660	Fully	Na_{Hg} , Na_{Sr}	300
mp-1047437	CaCu_2O_4	$I4_1/a$	0.644	Partially	Na_{Ca} , Ca_{Cu}	224
mp-5860	K_2HgO_2	$I4/mmm$	0.640	Fully	Na_{Hg}	160
mp-753287	CaCdO_2	$P4/mmm$	0.640	Fully	Na_{Cd} , Na_{Ca}	64
mp-5072	Rb_2HgO_2	$I4/mmm$	0.632	Fully	Na_{Hg}	160
mp-754326	NaAgO_2	$C2/m$	0.622	Partially	Ca_{Ag}	128
mp-3915	BaHgO_2	$R\bar{3}m$	0.618	Fully	Na_{Ba} , Na_{Hg}	300
mp-755478	CdBiO_3	$R3$	0.616	Lone-pair	–	–
mp-7232	Cs_2HgO_2	$I4/mmm$	0.616	Fully	Na_{Hg}	160
mp-23127	$\text{Ba}_2\text{BiSbO}_6$	$C2/m$	0.608	Lone-pair	–	–
mp-9158	LiCuO_2	$C2/m$	0.604	Partially	Ca_{Cu}	128
mp-1047036	CaAg_2O_4	$I4_1/a$	0.604	Partially	Ca_{Ag} , Na_{Ca}	122
mp-29164	SrBiO_3	$P2_1/c$	0.602	Lone-pair	–	–
mp-1224	HgO	$Pnma$	0.602	Fully	Na_{Hg}	96
mp-766217	$\text{Sr}_4\text{Cu}_2\text{O}_7$	$P2_1/c$	0.594	Partially	Na_{Sr} , Ca_{Cu}	104
mp-20015	As_2PbO_6	$P\bar{3}1m$	0.590	Lone-pair	–	–
mp-35647	Zn_2PtO_4	$Imma$	0.588	Fully	Na_{Zn} , Sc_{Pt}	122
mp-2133	ZnO	$P6_3mc$	0.588	Fully	Na_{Zn}	300

Table S2: Similar to Table S1 but for 33 oxides having w_{O-2p} smaller than that of ZnO and greater than 0.5. These oxides were only checked for shallow acceptor levels using PBEsol.

MP-ID	Formula	Space group	w_{O-2p}	Categories	Doping	N_{atoms}
mp-4541	NaCuO ₂	<i>C2/m</i>	0.584	Partially	Ca _{Cu}	64
mp-997088	KAgO ₂	<i>Cmcm</i>	0.580	Partially	Ca _{Ag}	128
mp-1096933	CsAgO ₂	<i>Cmcm</i>	0.580	Partially	Ca _{Ag}	128
mp-20727	Sb ₂ PbO ₆	<i>P$\bar{3}$1m</i>	0.578	Lone-pair	–	–
mp-7471	Li ₃ AuO ₃	<i>P4₂/mnm</i>	0.572	Partially	Ca _{Au}	224
mp-768915	Na ₃ AuO ₃	<i>P4₂/mnm</i>	0.564	Partially	Ca _{Au}	224
mp-782050	Ba ₄ PdO ₆	<i>R$\bar{3}$c</i>	0.564	Partially	Na _{Ba} , Sc _{Pd}	66
mp-23558	Ag ₂ BiO ₃	<i>Pnna</i>	0.560	Lone-pair	–	–
mp-1041631	Mg(CuO ₂) ₂	<i>Pbcm</i>	0.558	Partially	Na _{Mg} , Ca _{Cu}	224
mp-997052	RbAgO ₂	<i>Cmcm</i>	0.556	Partially	Ca _{Ag}	128
mp-8666	CsAgO	<i>I4/mmm</i>	0.552	Fully	–	–
mp-22984	NaBiO ₂	<i>C2/c</i>	0.552	Lone-pair	–	–
mp-1095378	AsAuO ₄	<i>C2/c</i>	0.548	Partially	Si _{As} , Sc _{Au}	194
mp-553310	CsCuO ₂	<i>Cmcm</i>	0.548	Partially	Ca _{Cu}	128
mp-22169	MoPbO ₄	<i>P$\bar{1}$</i>	0.544	Lone-pair	–	–
mp-29775	Sr ₄ PdO ₆	<i>R$\bar{3}$c</i>	0.540	Partially	Na _{Sr} , Sc _{Pd}	66
mp-8603	RbAgO	<i>I4/mmm</i>	0.540	Fully	–	–
mp-3982	KCuO ₂	<i>Cmcm</i>	0.540	Partially	Ca _{Cu}	96
mp-10299	Ca ₄ PdO ₆	<i>R$\bar{3}$c</i>	0.536	Partially	Na _{Ca} , Sc _{Pd}	66
mp-28796	Sr ₅ (AuO ₄) ₂	<i>I4/mmm</i>	0.536	Partially	Ca _{Au}	120
mp-997002	KAuO ₂	<i>Cmcm</i>	0.532	Partially	Ca _{Au}	96
mp-28365	Na ₃ AuO ₂	<i>P4₂/mnm</i>	0.528	Fully	–	–
mp-27253	Au ₂ O ₃	<i>Fdd2</i>	0.527	Partially	Ca _{Au}	120
mp-997089	NaAuO ₂	<i>Cmcm</i>	0.526	Partially	Ca _{Au}	96
mp-29920	Rb ₅ Au ₃ O ₂	<i>Pbam</i>	0.520	Fully	Ca _{Au}	120
mp-7472	RbAuO ₂	<i>Cmcm</i>	0.520	Partially	Ca _{Au}	96
mp-997024	CsAuO ₂	<i>Cmcm</i>	0.520	Partially	Ca _{Au}	96
mp-8727	Ba ₄ PtO ₆	<i>R$\bar{3}$c</i>	0.516	Partially	Na _{Ba} , Sc _{Pt}	66
mp-757242	Li ₅ AuO ₄	<i>Fddd</i>	0.516	Partially	Ca _{Au}	160
mp-760483	Li ₂ PdO ₃	<i>C2/m</i>	0.514	Partially	Sc _{Pd}	96
mp-559067	KNa ₂ AuO ₂	<i>Pnnm</i>	0.512	Fully	–	–
mp-557807	CsK ₂ AuO ₂	<i>Pnnm</i>	0.502	Fully	–	–
mp-997036	CdAuO ₂	<i>P$\bar{1}$</i>	0.500	Fully	Na _{Cd}	96

Table S3: List of 92 oxides having w_{O-2p} smaller than 0.5. Acceptor dopants for these oxides were not calculated.

Formula	w_{O-2p}	Formula	w_{O-2p}	Formula	w_{O-2p}
RbNa ₂ AuO ₂	0.498	Tl ₃ BO ₃	0.366	La ₂ Pd ₂ O ₅	0.196
CsAuO	0.496	Ba ₄ AgAuO ₆	0.364	LiCuO	0.184
Sr ₄ PtO ₆	0.496	LiAgO	0.356	CsCu ₃ O ₂	0.180
Sr(AuO ₂) ₂	0.488	CaAgAsO ₄	0.350	Cu ₂ PbO ₂	0.178
Ba(AuO ₂) ₂	0.488	Ca ₂ Pt ₃ O ₈	0.344	Ba ₂ Ca(PdO ₂) ₃	0.172
RbAuO	0.488	Na ₂ ReO ₃	0.340	Sr(CuO) ₂	0.160
Na ₃ CuO ₂	0.488	TiSnO ₃	0.320	CsCuO	0.160
LiAuO ₂	0.482	Tl ₃ AsO ₄	0.316	CuAsPbO ₄	0.156
KNa ₂ CuO ₂	0.480	LiAg ₃ O ₂	0.316	NaCuO	0.132
Mg ₂ PtO ₄	0.472	NaAg ₃ O ₂	0.312	AlCuO ₂	0.128
Na ₂ PtO ₃	0.464	Ag ₂ HgO ₂	0.304	Ba(CuO) ₂	0.124
Sr ₃ CdPtO ₆	0.460	Li ₂ PdO ₂	0.302	GaCuO ₂	0.124
Sr ₃ ZnPtO ₆	0.452	Na ₃ AgO ₂	0.300	KCuO	0.120
Tl ₂ Pt ₂ O ₇	0.452	AgAuO ₂	0.300	B ₆ O	0.118
Li ₈ PtO ₆	0.446	NaAgO	0.296	TlPd ₃ O ₄	0.112
Rb ₃ CuO ₂	0.440	AlAgO ₂	0.288	TiNb ₃ O ₆	0.108
Rb ₃ SbO ₃	0.433	BeTlAsO ₄	0.288	Zn(PtO ₂) ₃	0.098
Sr ₃ MgPtO ₆	0.420	Rb ₂ Sn ₂ O ₃	0.285	LaCuO ₂	0.096
RbCuO	0.420	LiNbO ₂	0.284	TlPt ₃ O ₄	0.056
Ca(AuO ₂) ₂	0.410	Hg ₂ WO ₄	0.276	LaZnAsO	0.050
In ₂ Pt ₂ O ₇	0.408	GaAgO ₂	0.272	Ca ₄ As ₂ O	0.046
Cs ₂ Pb ₂ O ₃	0.402	TlSbO ₃	0.264	La ₃ SbO ₃	0.044
K ₂ PdO ₂	0.398	K ₂ Sn ₂ O ₃	0.264	YZnAsO	0.044
Ba ₂ CePtO ₆	0.396	CaNb ₂ O ₄	0.256	Ca ₄ Sb ₂ O	0.042
Rb ₂ Pb ₂ O ₃	0.390	NaNbO ₂	0.256	Ca ₄ Bi ₂ O	0.041
La ₂ Pt ₂ O ₇	0.388	KAgO	0.244	Sr ₄ As ₂ O	0.035
Na ₂ PtO ₂	0.380	Tl ₂ SnO ₃	0.242	Sr ₄ Bi ₂ O	0.023
K ₂ Pb ₂ O ₃	0.378	ScAgO ₂	0.228	RbBa ₄ Sb ₃ O	0.000
Y ₂ Pt ₂ O ₇	0.376	Tl ₄ V ₂ O ₇	0.225	Ba ₃ BAsO ₃	0.000
Sc ₂ Pt ₂ O ₇	0.372	VAg ₃ HgO ₄	0.217	KBa ₄ Bi ₃ O	0.000
VAg ₃ O ₄	0.372	YAgO ₂	0.206		

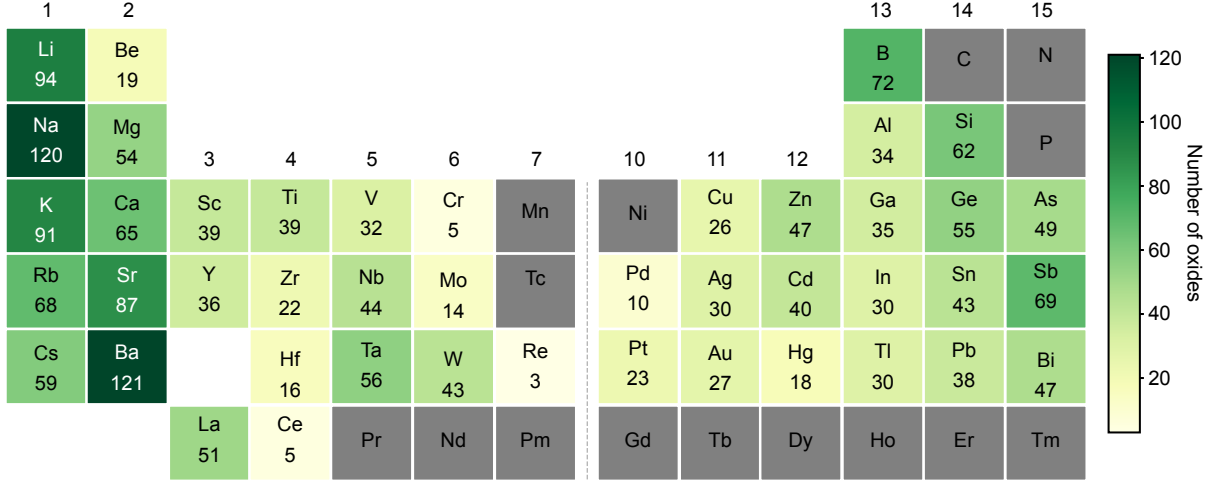


Figure S1: Number of oxides containing each element among the target 845 oxides.

Table S4: Representative p -type TCOs from the literature and the step at which each is excluded in this study are summarized. The Te containing oxides are excluded in the first step to avoid mixed-anion oxides. We then check the stability, oxygen vacancy formation energies, and the O-2 p contribution at the VBM. Details are described in the main text.

Oxides	Step to be excluded in this work					References
	Containing Te	Stability	$E_{f[V_O]}$	$w_{O-2p} < 0.588$	w_{O-2p}	
La_2O_2Te	✓				–	1
$\beta\text{-TeO}_2$	✓				–	2
SnO		✓			–	3
$Sb_4Cl_2O_5$		✓			–	4
CuLiO			✓		–	1
$CuAlO_2$				✓	0.128	5
B_6O				✓	0.118	6–8
$K_2Sn_2O_3$				✓	0.264	4
$K_2Pb_2O_3$				✓	0.378	4,8
Na_3AgO_2				✓	0.300	8
$Rb_2Pb_2O_3$				✓	0.390	8
$Cs_2Pb_2O_3$				✓	0.402	8
CsCuO				✓	0.160	1,8

References

- (1) Yim, K.; Youn, Y.; Lee, M.; Yoo, D.; Lee, J.; Cho, S. H.; Han, S. Computational discovery of p -type transparent oxide semiconductors using hydrogen descriptor. *npj Computational Materials* **2018**, *4*, 17.

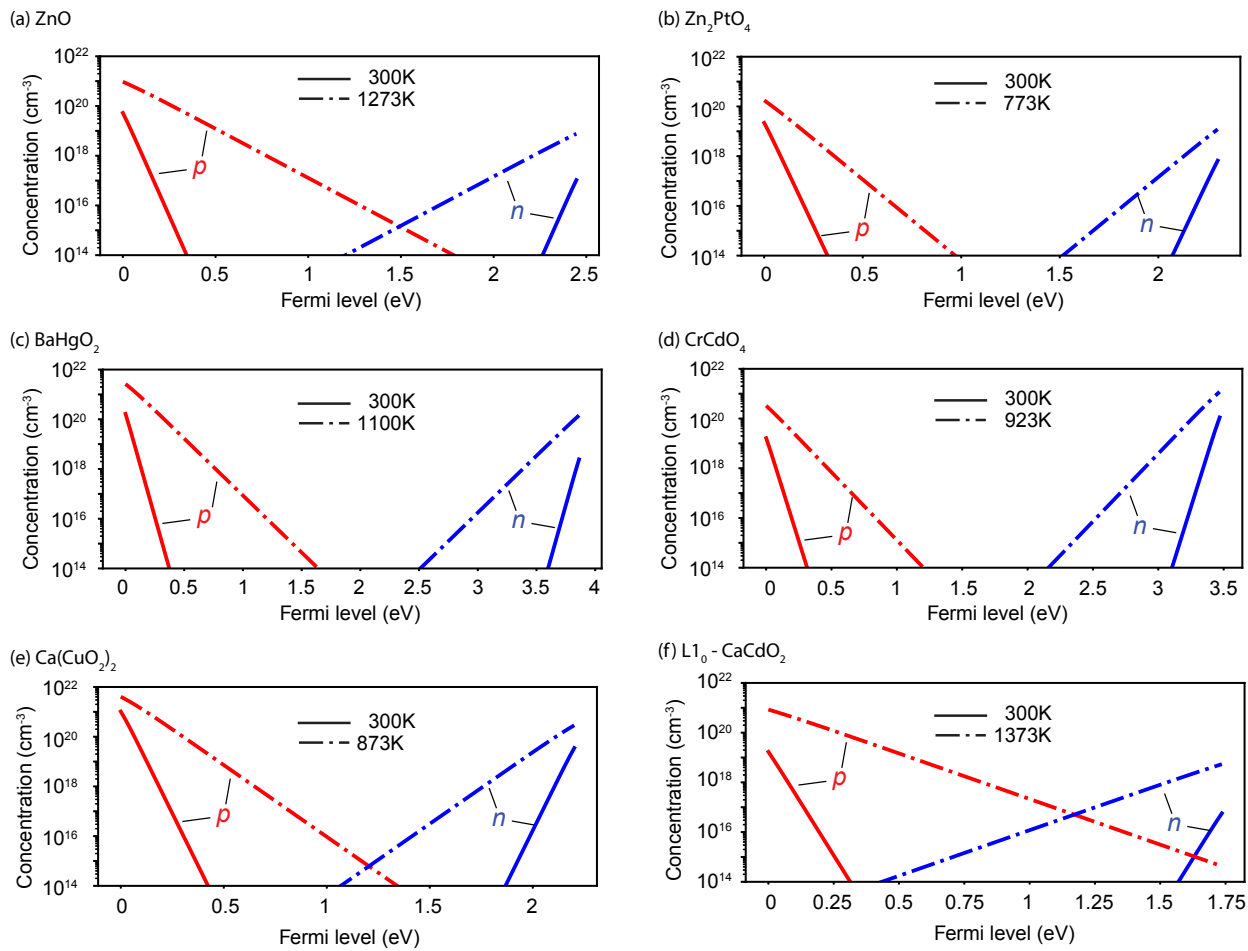


Figure S2: Carrier concentrations as a function of the Fermi level.

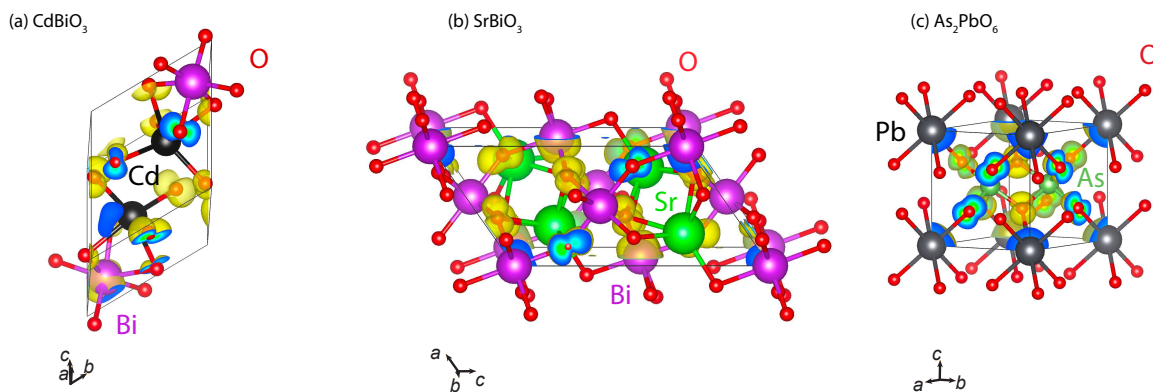


Figure S3: Isosurface plots of representative lone-pair oxides, each shown at 5% of the maximum electron density.

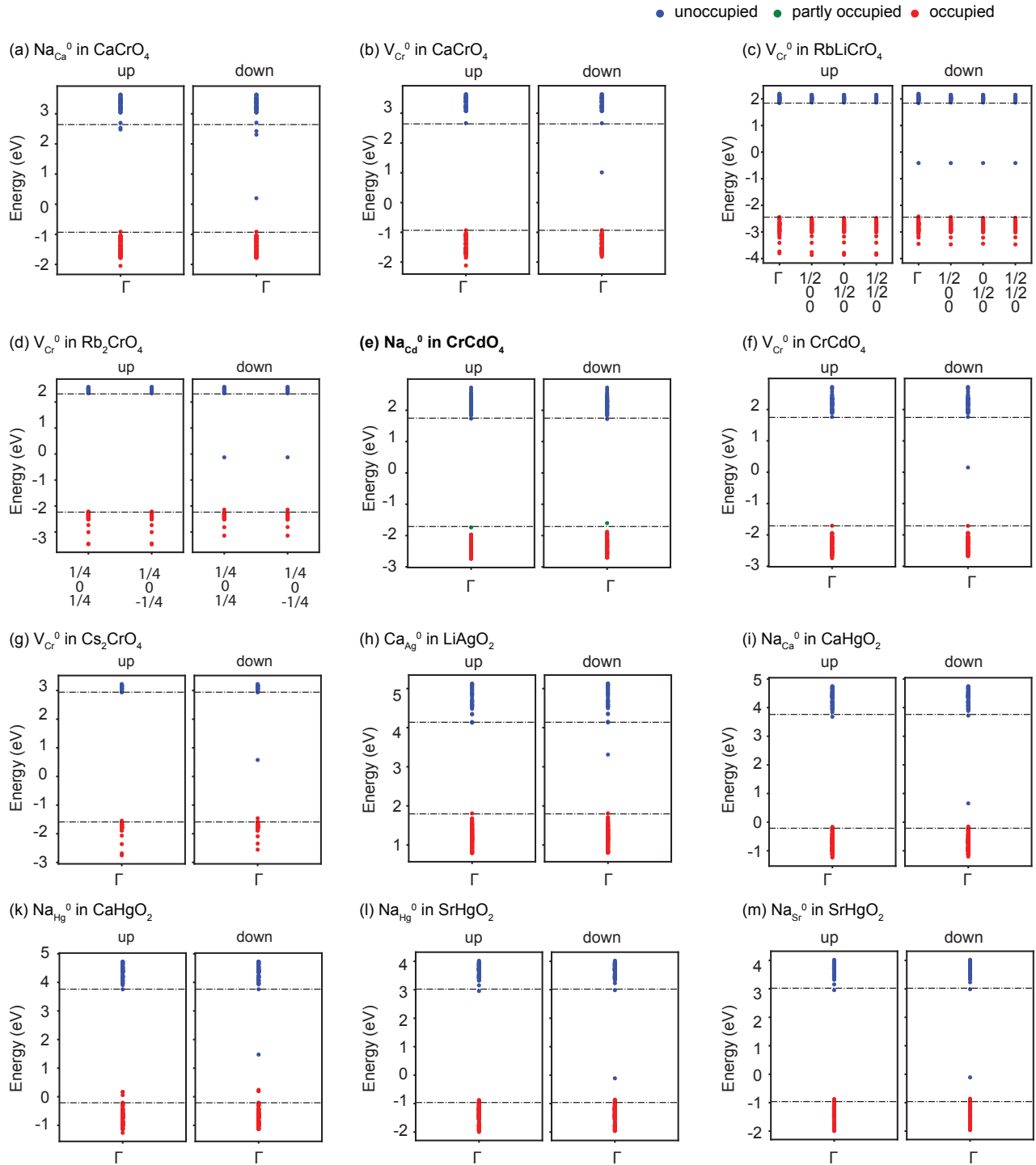


Figure S4: Single-particle levels of shallow acceptor dopants calculated using HSE06 for oxides that show shallow acceptor levels by dopants with PBEsol. **Bold** doping defects indicate those that remain shallow acceptors using HSE06. Both spin-up and spin-down levels are displayed for spin-polarized systems, while unpolarized systems are shown in a single panel. The vertical axis shown with absolute values.

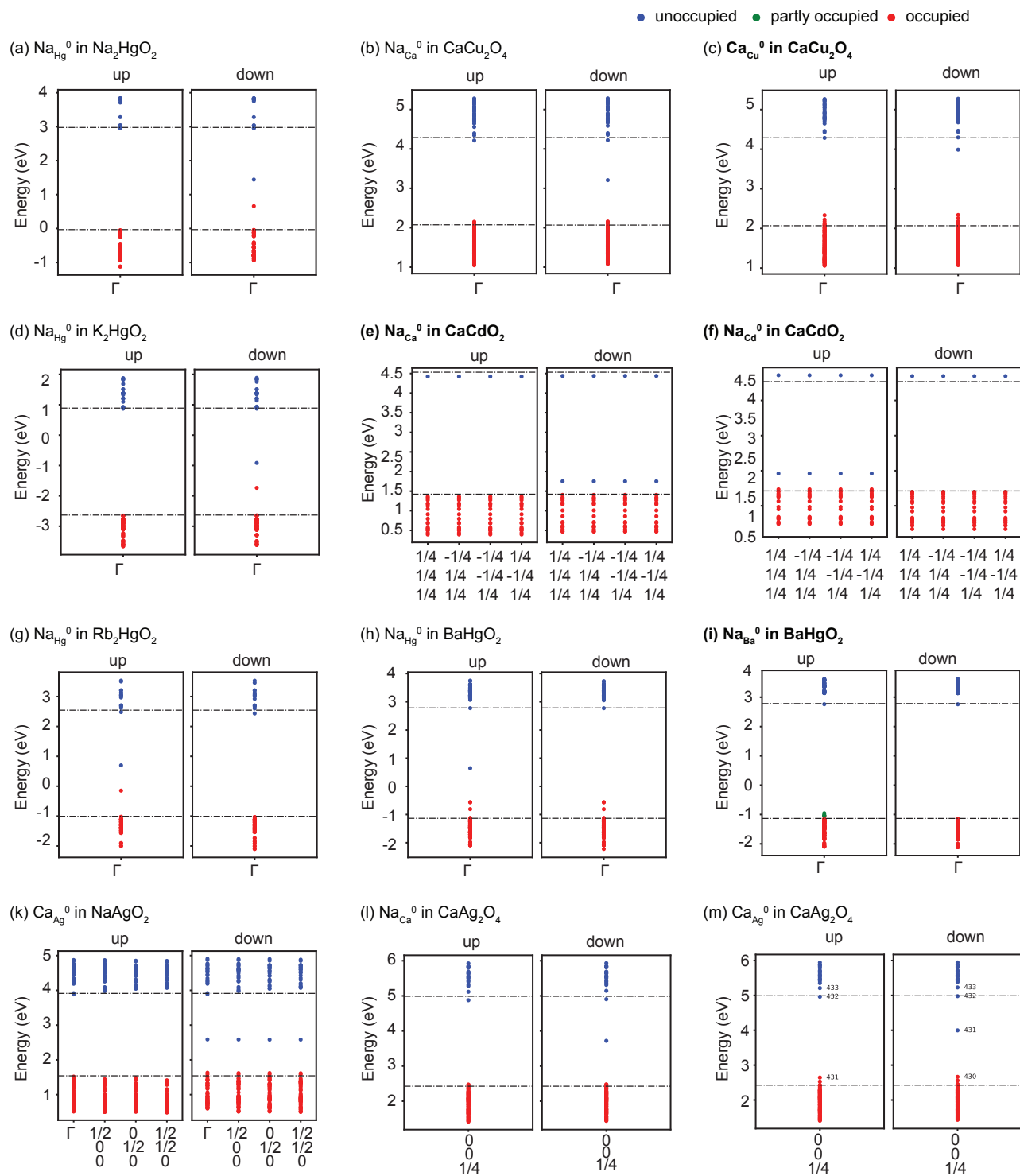


Figure S5: Continuation of Fig. S4.

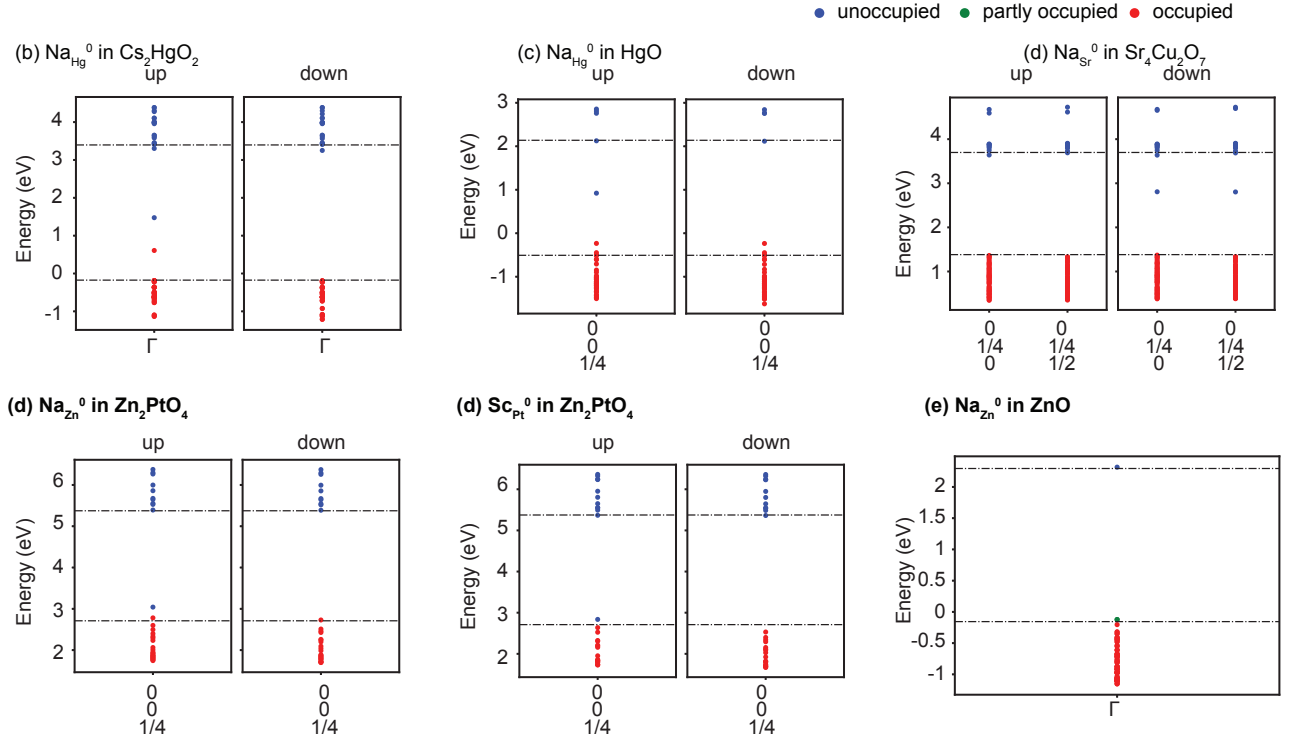


Figure S6: Continuation of Fig. S5.

Table S5: Crystal systems and hole effective masses of six candidates and SQS model.

Compound	Crystal system	$m_{h,x}^*$ (m_0)	$m_{h,y}^*$ (m_0)	$m_{h,z}^*$ (m_0)
ZnO	hexagonal	1.76	1.76	2.57
CrCdO ₄	orthorhombic	1.35	1.73	1.64
BaHgO ₂	rhombohedral	2.47	2.47	1.06
Zn ₂ PtO ₄	orthorhombic	0.83	4.22	1.83
CaCu ₂ O ₄	tetragonal	8.54	8.55	3.33
CaCdO ₂	tetragonal	1.62	1.62	0.42
sq _s -CaCdO ₂	cubic	1.83	1.88	1.83

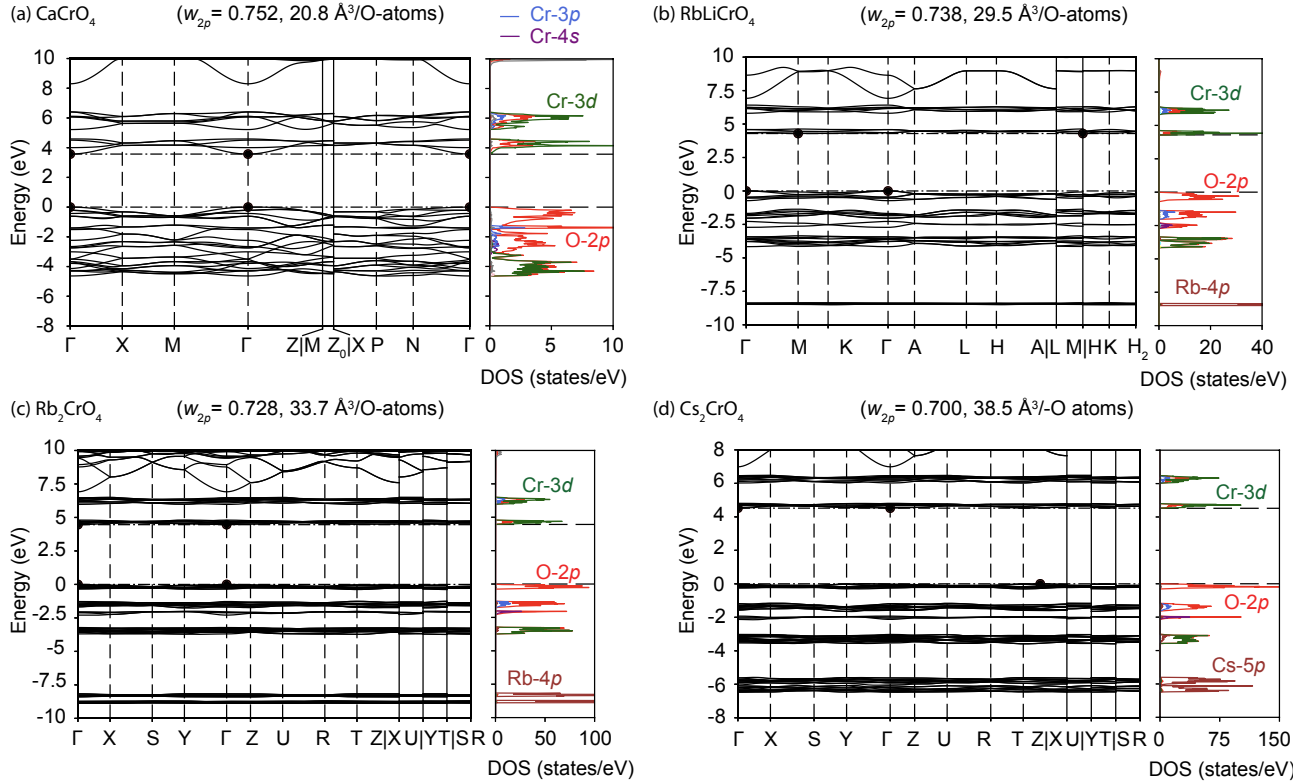


Figure S7: Electronic band structures and densities of state for four Cr-containing oxides. The O-2p contributions at the VBM (w_{O-2p}) and the unitcell volume per O-atoms are also shown in parentheses.

Table S6: Chemical potentials ($\Delta\mu_i$, where i means the impurity elements) of the ternary systems that include each impurity at points A (O-rich, Cr-poor), B, C (O-rich, Cd-poor), and D in CPD in Fig. S8 (a) for CrCdO_4 . The values are relative to those of the standard states, namely simple substances or molecules. The competing phases that include impurity elements are described.

	A-point	B-point	C-point	D-point
$\Delta\mu_{\text{Cd}}$	-2.11	-0.68	-4.17	-3.84
$\Delta\mu_{\text{Cr}}$	-6.72	-2.43	-4.66	-4.33
$\Delta\mu_{\text{O}}$	0.0	-1.43	0.0	-0.16
$\Delta\mu_{\text{Na}}$	-3.17	-2.46	-5.71	-5.39
Competing phase	CdO, O ₂ (g)	CdO, Cr ₂ O ₃	CrO ₂ , O ₂ (g)	Cr ₂ O ₃ , CrO ₂
Impurity phase	Na ₂ CrO ₄	Na ₂ CrO ₄	NaCr ₃ O ₈	NaCr ₃ O ₈

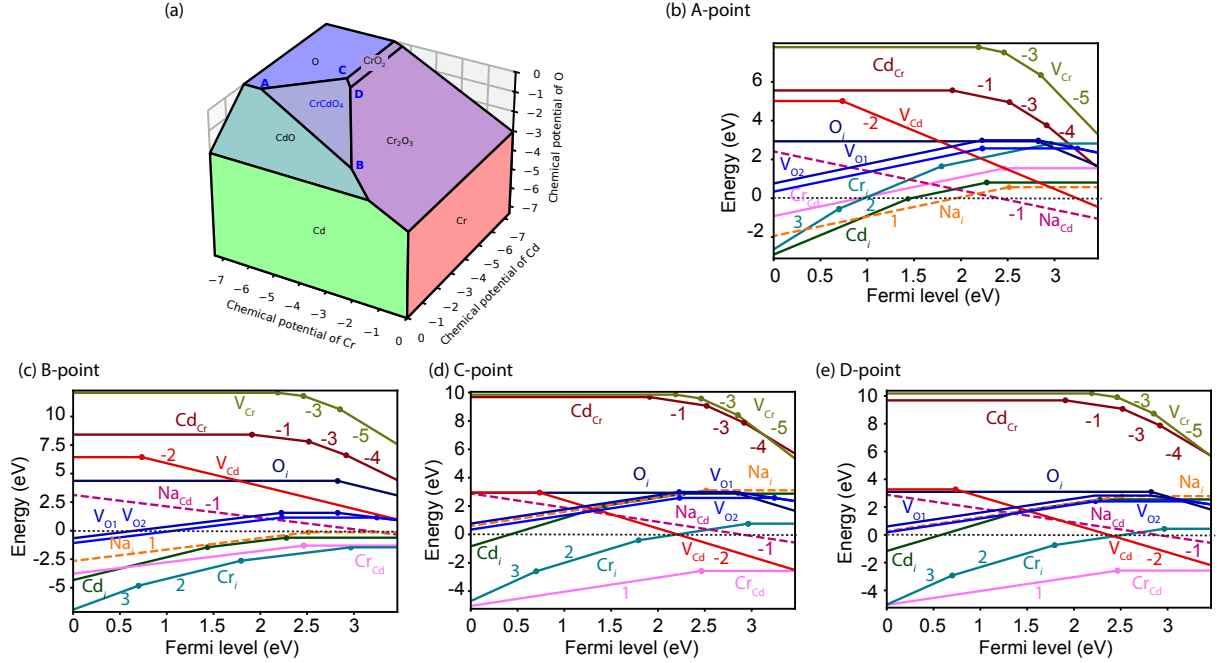


Figure S8: (a) Chemical potential diagram of Cr-Cd-O ternary system. (b-e) Formation energies of native defects and Na dopants in CrCdO_4 as function of the Fermi level at A, B, C, D chemical potentials.

Table S7: Same as Table. S6 but for points A, B, C, and D in CPD in Fig. S9 (a) for CaCdO_2 .

	A-point	B-point	C-point	D-point
$\Delta\mu_{\text{Ca}}$	-4.00	-6.15	-4.02	-6.16
$\Delta\mu_{\text{Cd}}$	0.0	-2.15	0.0	-2.14
$\Delta\mu_{\text{O}}$	-2.15	0.0	-2.14	0.0
$\Delta\mu_{\text{Na}}$	-0.98	-2.28	-0.94	-2.28
Competing phase	Ca_3CdO_4 , Cd	Ca_3CdO_4	CaCd_3O_4 , Cd	CaCd_3O_4 , $\text{O}_2(\text{g})$
Impurity phase	Na_2CdO_2	Na_2O_2	Na_2CdO_2	Na_2O_2

Table S8: Considered competing phases for CrCdO_4 .

Competing phases	
CrCdO_4	$\text{O}_2(\text{g})$, Cd, CdO, Cr, Cr_2CdO_4 , Cr_2O_3 , CrCdO_4 , CrO_2
Na	Na, $\text{Na}_{14}\text{Cd}_2\text{O}_9$, Na_2CdO_2 , $\text{Na}_2\text{Cr}_2\text{O}_7$, Na_2CrO_4 , $\text{Na}_2\text{ONa}_2\text{O}_2$, Na_3Cd , NaCd_3 , NaCr_3O_8 , NaCrO_2 , NaO_2

(2) Huyen, V. T. N.; Bae, S.; Costa-Amaral, R.; Kumagai, Y. Native defects and p -type dopability in transparent $\beta\text{-TeO}_2$: A first-principles study. *Phys. Rev. Appl.* **2024**, *22*,

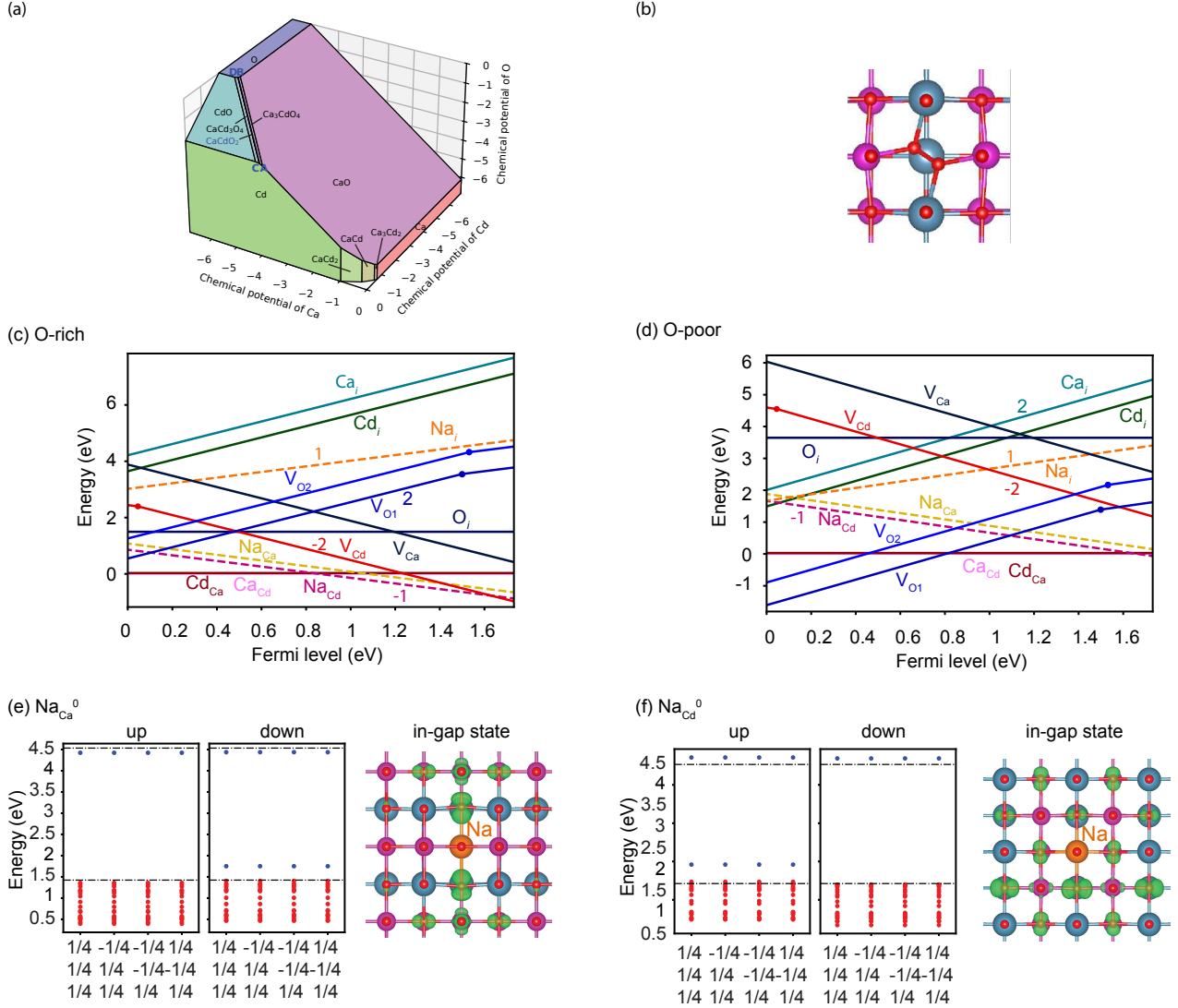


Figure S9: (a) Chemical potential diagram (CPD) of Ca-Cd-O ternary system. (b) Dimer structure for oxygen interstitial. (c-d) Formation energies of native defects and Na dopants in L1_0 - CaCdO_2 as function of the Fermi level at oxygen-rich (B) and oxygen-poor (A) chemical potentials. (e-f) Single-particle levels at some k -points in the L1_0 - CaCdO_2 and the corresponding of the squared wave functions for the in-gap states for the defect Na_{Ca}^0 and Na_{Cd}^0 . Isosurfaces correspond to 5% of the maxima in each case.

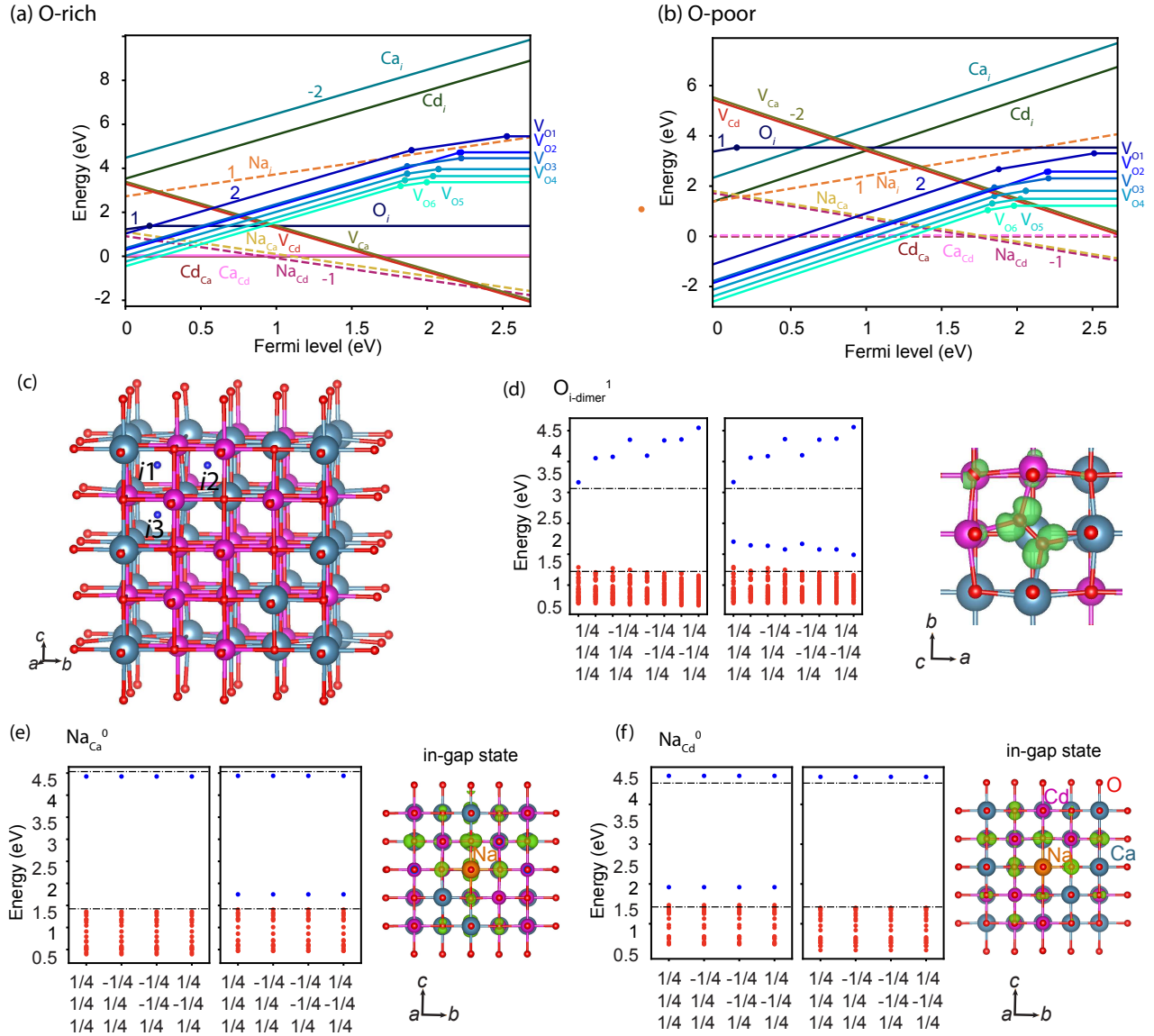


Figure S10: (a-b) Formation energies of native defects and Na dopants in SQS-CaCdO₂ model as function of the Fermi level at oxygen-rich (B) and oxygen-poor (A) chemical potentials. (c) Crystal structure with the interstitial sites are shown as a black spheres. (d) Single-particle levels at some k -points in the supercell models in dimer structure for oxygen interstitial defect with charge +1 and the corresponding of the squared wave functions for in-gap state. (e-f) Similar (d) but for Na_{Ca}⁰ and Na_{Cd}⁰.

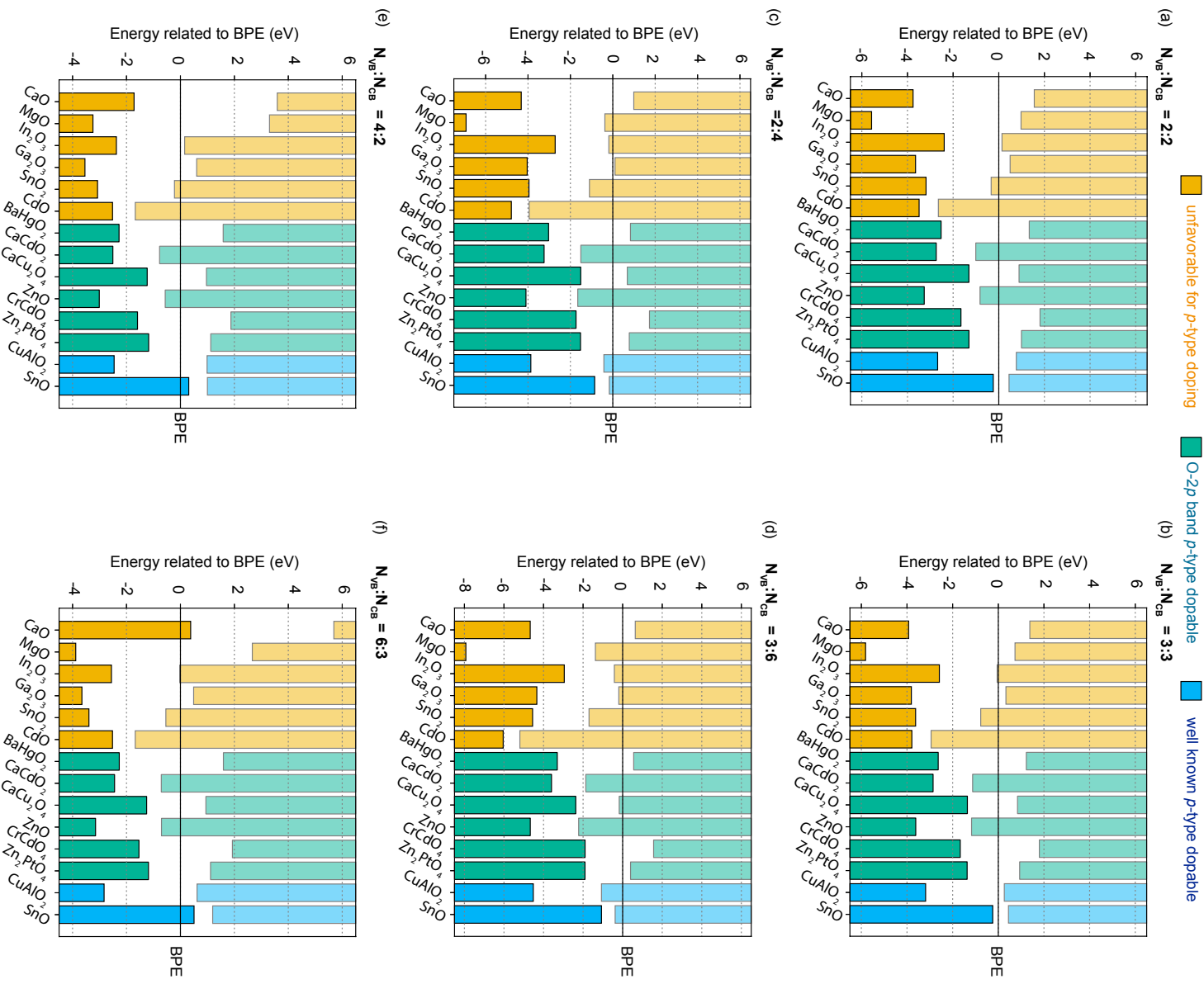


Figure S11: Band alignment obtained using HSE06, showing VBM across three group type the same Fig. 6 in main text but aligned to branch point energy (BPE) with changing number of bands averaged over in valence band (N_{VB}) and in conduction band (N_{CB}).

Table S9: Considered competing phases for CaCdO₂.

Competing phases	
CaCdO ₂	O ₂ (g), Ca, Ca ₃ Cd ₂ , Ca ₃ CdO ₄ , CaCd, CaCd ₂ , CaCd ₃ O ₄ , CaCdO ₂ , CaO, Cd, CdO
Na	Na, Na ₁₄ Cd ₂ O ₉ , Na ₂ CdO ₂ , Na ₂ O, Na ₂ O ₂ , Na ₃ Cd, NaCd ₃ , NaO ₂

Table S10: Calculated sites for Na-substitution defects, cation vacancies, cation interstitials, and oxygen-dimer interstitials in the CaCdO₂ SQS model.

Sites	Fractional coordinates
Cd1	(1, 1/2, 1/2)
Cd2	(0, 1/2, 0)
Cd3	(1/2, 1/2, 1/2)
Ca1	(1, 0, 1/2)
Ca2	(1, 0, 1)
Ca3	(1/2, 1, 1/2)
Na _{i1} , Ca _{i1} , Cd _{i1}	(3/8, 1/8, 5/8)
Na _{i2} , Ca _{i2} , Cd _{i2}	(3/8, 1/8, 7/8)
Na _{i3} , Ca _{i3} , Cd _{i3}	(3/8, 3/8, 7/8)
O-dimer1	(-0.05, 0.05, 0.255), (0.05, -0.05, 0.245)
O-dimer2	(0.05, -0.05, 0.755), (-0.05, 0.05, 0.745)
O-dimer3	(0.05, 0.55, 0.255), (0.05, 0.45, 0.245)

Table S11: Calculated equilibrium Fermi level from the valence band maximum, defect, and carrier concentrations under the O-rich conditions at 1373 K in L1₀-CaCdO₂ are provided in units of cm⁻³.

T (K)	E_f (eV)	p	n	Ca _{Cd} ⁰	Cd _{Ca} ⁰	Na _{Cd} ⁻¹	Na _{Ca} ⁻¹	V _{O1} ²⁺
1373	0.268	1×10^{20}	5×10^{13}	2×10^{22}	2×10^{22}	1×10^{20}	2×10^{19}	2×10^{18}

044065.

- (3) Varley, J. B.; Schleife, A.; Janotti, A.; Van de Walle, C. G. Ambipolar doping in SnO. *Appl. Phys. Lett.* **2013**, *103*, 082118.
- (4) Hautier, G.; Miglio, A.; Ceder, G.; Rignanese, G.-M.; Gonze, X. Identification and design principles of low hole effective mass p -type transparent conducting oxides. *Nat. Commun.* **2013**, *4*, 2292.
- (5) Kawazoe, H.; Yasukawa, M.; Hyodo, H.; Kurita, M.; Yanagi, H.; Hosono, H. P -type

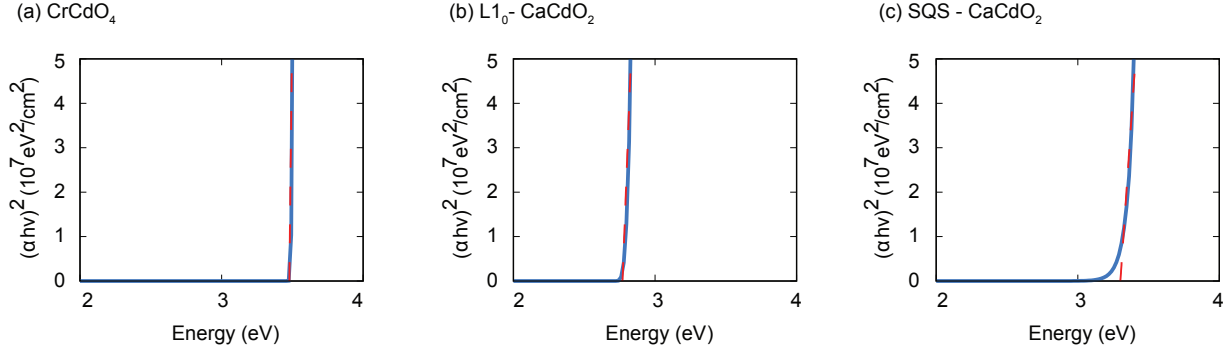


Figure S12: Tauc plots for the CrCdO_4 , $\text{L1}_0\text{-CaCdO}_2$ and SQS-CaCdO_2 .

electrical conduction in transparent thin films of CuAlO_2 . *Nature* **1997**, *389*, 939–942.

- (6) Varley, J. B.; Lordi, V.; Miglio, A.; Hautier, G. Electronic structure and defect properties of B_6O from hybrid functional and many-body perturbation theory calculations: A possible ambipolar transparent conductor. *Phys. Rev. B* **2014**, *90*, 045205.
- (7) Akashi, T.; Itoh, T.; Gunjishima, I.; Masumoto, H.; Goto, T. Thermoelectric Properties of Hot-pressed Boron Suboxide (B_6O). *Materials Transactions* **2002**, *43*, 1719–1723.
- (8) Kumagai, Y. Computational Screening of p -Type Transparent Conducting Oxides Using the Optical Absorption Spectra and Oxygen-Vacancy Formation Energies. *Phys. Rev. Appl.* **2023**, *19*, 034063.